Natural Resources Canada | Ressources naturelles Canada

GEOLOGICAL SURVEY OF CANADA
OPEN FILE 9176

U-Pb ID-TIMS zircon geochronology for selected Archean intrusive rocks associated with gold deposits of Quebec and Ontario

B. Dubé, P. Mercier-Langevin, M.A. Hamilton, N. Wodicka, V.J. McNicoll, A. Fontaine, and D.J. Kontak

2024

Canada

GEOLOGICAL SURVEY OF CANADA
OPEN FILE 9176

U-Pb ID-TIMS zircon geochronology for selected Archean intrusive rocks associated with gold deposits of Quebec and Ontario

B. Dubé[1], P. Mercier-Langevin[1,2], M.A. Hamilton[3], N. Wodicka[4], V.J. McNicoll[4], A. Fontaine[5], and D.J. Kontak[6]

[1]Geological Survey of Canada, 490, rue de la Couronne, Québec, Québec
[2]Present address: Agnico Eagle Mines Limited, 145 King Street East, Toronto, Ontario
[3]Jack Satterly Geochronology Laboratory, University of Toronto, 22 Russell Street, Toronto, Ontario
[4]Geological Survey of Canada, 601 Booth Street, Ottawa, Ontario
[5]Institut national de la Recherche scientifique, Centre Eau Terre Environnement, 490, rue de la Couronne, Québec, Québec
[6]Harquail School of Earth Sciences, Laurentian University, 935 Ramsey Lake Road, Sudbury, Ontario

2024

Permanent link: https://doi.org/10.4095/p47mbq986y

This publication is available for free download through the NRCan Open Science and Technology Repository (https://ostrnrcan-dostrncan.canada.ca/).

Recommended citation
Dubé, B., Mercier-Langevin, P., Hamilton, M.A., Wodicka, N., McNicoll, V.J., Fontaine, A., and Kontak, D.J., 2024. U-Pb ID-TIMS zircon geochronology for selected Archean intrusive rocks associated with gold deposits of Quebec and Ontario; Geological Survey of Canada, Open File 9176, 47 p. https://doi.org/10.4095/p47mbq986y

Publications in this series have not been edited; they are released as submitted by the author.

ISSN 2816-7155
ISBN 978-0-660-71354-0
Catalogue No. M183-2/9176E-PDF

U-Pb ID-TIMS zircon geochronology for selected Archean intrusive rocks associated with gold deposits of Quebec and Ontario

B. Dubé[1], P. Mercier-Langevin[1,2], M.A. Hamilton[3], N. Wodicka[4], V.J. McNicoll[4], A. Fontaine[5], and D.J. Kontak[6]

[1]Geological Survey of Canada, 490, rue de la Couronne, Québec, Québec
[2]Present address: Agnico Eagle Mines Limited, 145 King Street East, Toronto, Ontario
[3]Jack Satterly Geochronology Laboratory, University of Toronto, 22 Russell Street, Toronto, Ontario
[4]Geological Survey of Canada, 601 Booth Street, Ottawa, Ontario
[5]Institut national de la Recherche scientifique, Centre Eau Terre Environnement, 490, rue de la Couronne, Québec, Québec
[6]Harquail School of Earth Sciences, Laurentian University, 935 Ramsey Lake Road, Sudbury, Ontario

*Corresponding author email: ben_dube@sympatico.ca

ABSTRACT

The Superior Province hosts several major types and styles of gold deposits. The controls on the formation of these various types of gold deposits are generally relatively well understood, although the exact timing of gold introduction remains unclear in many cases. Field relationships combined with precise geochronology remain the best elements in constraining the age of formation of a deposit, which allows to associate ore-forming activity with specific geological events, helping refine exploration and genetic models. This report presents U-Pb geochronological results from dating of igneous zircon from selected intrusive rocks of the Abitibi greenstone belt and La Grande subprovince that are associated with gold deposits.

Intrusive rocks from the Bachelor (O'Brien intrusion: 2692.1 ± 2.0 Ma), Timmins West complex (HWY-144 - 144 GAP host syenite intrusion: 2679.7 ± 1.6 Ma), Black Fox (pre-ore "albitite" dyke: 2702.3 ± 0.89 Ma), and Macassa (host syenite porphyry: 2676.6 ± 1.1 Ma) mines, and from the Upper Beaver (post-ore diorite "spotted porphyry" dyke: 2678.7 ± 0.7 Ma) and Cheechoo (host intrusion: 2612.3 ± 0.8 Ma) deposits were dated. Samples from the Francoeur, Thunder Creek deposit (Timmins West complex) and Macassa mines were analyzed as well but did not yield ages. The ages on intrusive rocks spatially associated with gold deposits presented in this report help clarify the relationship between major gold ore-forming events and specific magmatic and tectonometamorphic events related to the evolution of the Abitibi greenstone belt and La Grande subprovince.

INTRODUCTION

This report presents U-Pb geochronological results from isotope dilution-thermal ionization mass spectrometry (ID-TIMS) dating of zircon from selected intrusive rocks of the Abitibi greenstone belt and La Grande subprovince. The dated intrusive rocks host and/or are associated with gold deposits and provide constraints, both maximum and minimum, on the timing of mineralization in selected areas. The work presented here was initiated by the Geological Survey of Canada through Targeted Geoscience Initiative (TGI) Abitibi (TGI-3), Lode Gold (TGI-4: Dubé and Mercier-Langevin, 2015), and Gold (TGI-5: Mercier-Langevin et al., 2020) projects and as part of its review of gold metallogeny in the Abitibi greenstone belt (see Dubé and Mercier-Langevin, 2020). This work was done in collaboration with the Jack Satterly Geochronology Laboratory (University of Toronto), the provincial surveys (Ministère des Ressources naturelles et des Forêts and Ontario Geological Survey), and the industry. The objective of this study was to improve the current knowledge of such intrusion-associated deposits by adding critical age constraints on a variety of styles of gold mineralization and deposits in major Archean gold districts. Geochronology results and their implications are briefly reported and discussed here. Although previously reported in the literature, most of the U-Pb ages presented here were never formally published with precise information regarding the samples, locations and compositions, and complete analytical data (e.g. data tables, concordia diagrams.

SAMPLE SELECTION AND DESCRIPTIONS

Eight samples were selected to better constrain the timing of gold mineralization in the Abitibi greenstone belt as different types of deposits and different styles of mineralized zones occur at belt scale, in varied settings, with a significant spread in time, as documented in detail in Dubé and Mercier-Langevin (2020). The samples come from the Chibougamau district (Bachelor mine), Timmins-Porcupine district (Timmins West complex), Matheson camp (Black Fox), Rouyn-Noranda district (Francoeur mine area), Kirkland Lake district (Macassa mine), and Larder Lake camp (Upper Beaver deposit) as shown in Figure 1. A nine sample was collected at the Cheechoo gold property in the Eeyou Istchee James Bay region, 15 km southeast of the Éléonore gold mine, near the contact between the La Grande and Opinaca subprovinces (Fig. 2). Following are detailed descriptions of each sample along with lithogeochemical characteristics (see Table 1 for whole-rock major and trace element data).

Sample BFBD-2016-001 is from an aphanitic, pre-ore dyke emplaced within highly-strained ultramafic rocks at the Black Fox mine, Matheson area (Fig. 1). Gold mineralization at the Black Fox Mine is hosted by orogenic quartz-carbonate fault-fill and extensional veins in sheared ultramafic and mafic volcanic rocks (Brisson, 2014; Kelly, 2021). The dated sample was taken at the 680 level (Deep Central zone: 10335E and 9775N in local mine grid: Fig. 3) by D. Rhys (Panterra Geoservices) and Primero Mining geologists. It consists of an altered (bleached) unit that contains a developed hydrothermal alteration-related assemblage including albite, sericite, Fe and Mg carbonate, pyrite, and quartz (Fig. 4A, B). Pyrite (5-10%) occurs as fine disseminations (<1 mm) throughout as replacement-style mineralization within areas of Fe-Mg carbonate alteration. Traces of dark green chlorite ±amphibole aggregates and veinlets are locally present in the sample (Fig. 4A, B). The dyke is weakly to moderately strained and cut by mineralized quartz-carbonate veins (6.32 g/t Au: Table 1) oriented at a high-angle or subparallel to the main foliation (S_3) (Fig.

4A). It is andesitic to dacitic in composition (Fig. 5A) and plots at the transition between the quartz-monzonite, monzonite and syenite fields in figure 5B, although the dated sample is strongly altered. Its trace element signature is that of other evolved intrusive rocks with a negative Nb, Ta and Ti anomalies, and enrichment in high-field strength elements (HFSE), with a light rare earth (LREE) enriched [(La/Lu)N ≈ 10) but flat heavy rare-earth profile (Fig. 6A, B). This dyke is possibly equivalent to "albitite" dykes described elsewhere in the Abitibi belt along the Destor-Porcupine and Larder Lake-Cadillac fault zones (Fig. 1; Dubé and Mercier-Langevin, 2020), which likely represent a series of different dyke compositions and ages that have been preferentially affected by albitic alteration in altered areas. Kelly (2021) presents detailed information about the various types of pre-ore dykes at the Black Fox Mine.

Sample PLBD-2018-019 is from the O'Brien intrusion that is strongly porphyritic with large (up to 3-4 cm) feldspar phenocrysts (Fig. 4C, D). The O'Brien intrusion hosts a minor part of the gold-bearing zones at the Bachelor mine located near the village of Desmaraisville in northeastern Abitibi greenstone belt (Buro, 1984; Fig. 1). The mineralization is mainly hosted in three planar replacement zones within the massive, brecciated and pillowed basaltic to andesitic flows and intermediate to felsic volcaniclastic rocks of the Obatogamau Formation, which are cut by the O'Brien stock (Buro, 1984; Lauzière, 1989; Fayol and Jébrak, 2017; Dubé and Mercier-Langevin, 2020). The intrusion is pinkish to reddish in colour and locally cut by mineralized veins (Fig. 4C). The dated sample was taken underground at the Bachelor mine, in stope 14-03, along the "track-drift", near the intersection of the A and Main ore zones (Level 14, 14710E, 9610N in local mine grid: Fig. 7). Although the intrusion is locally cut by structurally controlled mineralized quartz veins and appears hematized (Fig. 4C, D), the dated sample is weakly altered with minor sericite and carbonate in a fine-grained matrix (Fig. 4D, E) and contains 100 ppb Au (Table 1). It has a felsic composition (Fig. 5A) and plots as a granite in Middlemost (1994) total alkali silica (TAS) diagram, with an alkaline affinity comparable to that of early- to syn-Timiskaming alkaline/shoshonitic to sub-alkaline intrusive rocks (Dubé and Mercier-Langevin, 2020; Fig. 5B). The normalized multi-element spider diagram (Pearce 2008) shows enrichment in less mobile high field strength elements (HFSE), and strong Nb, Ta, and Ti negative anomalies (Fig. 6B) in agreement with the analyses presented in Fayol and Jébrak (2017) and Dubé and Mercier-Langevin (2020) for the O'Brien intrusion. Detailed information about the Bachelor deposit and its geology are given in Buro (1984), Lauzière (1989), Fayol and Jébrak (2017), and Dubé and Mercier-Langevin (2020).

Sample PLDB-2018-039 is from a shear zone-hosted, foliated pre-mineralization "albitite" dyke exposed to surface in trench No. 8 along the Francoeur mine site access road (UTM NAD83 Zone 15, 628 260 m E, 5 340 675 m N: Fig. 4F). The Francoeur deposit, a few kilometers west of the city of Rouyn-Noranda (Fig. 1), is described in detail in Couture and Pilote (1993). The sampled dyke is fine-grained with a strongly sericite, albite, and iron carbonate-altered groundmass and contains abundant fine-grained disseminated pyrite (Fig. 8A, B). The sample has almost 10% CO_2 and 5% total S, indicating it is strongly carbonatized and sulfidized (mainly pyrite) (Table 1). It is andesitic in composition and plots as a monzodiorite (Fig. 5A, B), although the sample is intensely altered. It has a relatively flat REE pattern and strong Nb, Ta, and Ti anomalies (Fig. 6A, B). The dyke is deformed and located in the "Main Shear" mineralized zone that is hosted in strongly foliated and iron carbonate-altered intermediate volcanic rocks (Fig. 4F). A grab sample of the dyke gave a value of 6.08 g/t Au (Table 1).

Sample PLDB-2018-052 is from a gold-bearing syenite porphyry intrusion with feldspar microphenocrysts at the Thunder Creek deposit, porphyry zone, Timmins West complex (Fig. 1). The geology of the Timmins West complex is detailed in Campbell (2014) and Kallio and Vaz (2016). The sample was taken on level 785, along access drift No. 4. The intrusion is hematite-(orangy to reddish) and sericite altered and cut by abundant shallowly dipping quartz ±pyrite gold-bearing veins (Fig. 8C). Petrography (Fig. 8D) and whole rock lithogeochemistry (Table 1) indicate that the intrusion is moderately altered despite the coloration and abundant veining (Fig. 8C). The dated sample is felsic (rhyodacitic in composition: Fig. 5A) and plots as a granite, at the transition between the alkaline and sub-alkaline fields in Middlemost (1994) TAS diagram (Fig. 5B). More information about the Thunder Creek deposit is given in Campbell (2014), Kallio and Vaz (2016), van Kessel (2018), and Dubé and Mercier-Langevin (2020).

Sample PLDB-2018-056 is from a syenite porphyry at the HWY-144 (144 GAP) deposit of the Timmins West complex (Fig. 1). The sampled syenite porphyry contains very abundant and large, zoned K-feldspar phenocrysts (Fig. 8E, F) and hosts the ore zone at the HWY-144 (144 GAP) deposit. It was sampled at the 890 level, W-POR#15 stope. Although barren and weakly altered on visual inspection (Figs. 8E, 9A), whole-rock lithogeochemistry suggests that carbonate-alteration is significant in the sample (Table 1). It is intermediate to felsic in composition (Fig. 5A) and plots as a syenite in Middlemost (1994) TAS diagram (Fig. 5B), which agrees with the composition of least-altered samples analyzed in Dubé and Mercier-Langevin (2020). The normalized multi-element spider diagram, which uses elements that are considered less mobile, shows high light rare-earth elements relative to heavy rare-earths, strong Nb, Ta, and Ti negative anomalies, and the absence of an Eu anomaly, which are characteristic of syn-Timiskaming alkaline/shoshonitic to sub-alkaline intrusions (Fig. 6A, B).

Sample BDPL-KL-2018-202 is from the syenite porphyry at the Macassa mine, immediately adjacent 04 Break in the Kirkland Lake camp (Fig. 1). This sample, from the 3338' elevation on the 3423 incline, consists of moderately- to strongly-altered syenite porphyry, purple to reddish in colour (Fig. 9B). The sample was collected by S. Farrell (Kirkland Lake Gold) and D. Rhys (Paterra Geoservices). The syenite porphyry hosts ore at the Macassa mine and is the main host of the giant Kirkland Lake deposit (see Ispolatov et al., 2008 and references therein, for details about the geology of the Macassa deposit). Although barren, the sample is cut by traces of quartz veinlets and fracture-controlled iron carbonate alteration (Fig. 9B) as shown by its chemical composition (60.9 wt.% CO_2: Table 1). The selected sample plots as a quartz-monzonite in Middlemost (1994) TAS diagram (Fig. 5B), with a subalkaline to slightly alkaline affinity, similar to least-altered analyses from the syenite porphyry reported in Ispolatov et al. (2008) and Dubé and Mercier-Langevin (2020). According to Hicks (1990), the syenite porphyry has a composition that varies from quartz monzonite/quartz monzodiorite to granodiorite. The normalized multi-element spider diagram shows strong enrichment in HFSE elements, and strong Nb, Ta, and Ti negative anomalies. Such signature characterized syn-Timiskaming alkaline/shoshonitic to sub-alkaline intrusions (Fig. 6B).

Sample BDPL-KL-2018-201 was collected from the 3000' elevation on the 3422 incline, approximately 195 feet south of the 04 Break at the Macassa mine. The sample was collected by S. Farrell (Kirkland Lake Gold) and D. Rhys (Paterra Geoservices). It consists of massive to locally weakly foliated, dark grey, least-altered, feldspar-phyric syenite porphyry (Fig. 9C), and is host to

ore. The unit is characterized by 4–6% euhedral and feldspar phenocrysts (1–4 mm), with minor mafic clasts 1–2 cm in size (Fig. 9C). The sample is barren and is chemically less altered than sample BDPL-KL-2018-202 (Table 1). The dated sample plots as a quartz-monzonite in Middlemost (1994) diagram (Fig. 5B), with a subalkaline to slightly alkaline affinity, similar to least-altered analyses from the syenite porphyry in Ispolatov et al. (2008) and Dubé and Mercier-Langevin (2020). As for sample BDPL-KL-2018-202, the normalized multi-element spider diagram shows patterns similar to the syn-Timiskaming alkaline/shoshonitic to sub-alkaline intrusions (Fig. 6B).

Sample UB-07-157 was collected from drill core UB-07-98 (570 m depth: Fig. 10) from a thick intersection of feldspar “syenite”, locally referred to as the "spotted porphyry", that crosscuts all mineralized zones at the Upper Beaver Cu-Au deposit (Fig. 1) and is recognized as the latest pulse of the Upper Beaver intrusive magmatism in the area. Although often called a porphyry and/or syenite, this intrusive unit is a plagioclase- and amphibole-phyric diorite. The selected sample straddles the transition between the monzonite, quartz-monzonite, and diorite fields in Middlemost (1994) diagram (Fig. 5B). The "spotted porphyry" is an intrusive phase (Table 1) consisting of a large WNW-ESE-oriented dyke that cuts earlier intrusive phases such as the “mafic” and “crowded” porphyries (Fig. 10; Kontak et al., 2008; Feick, 2016). The sample is a fine-grained, red-brown intermediate rock with 5 to 7 vol %, equant, subhedral to euhedral feldspar grains (<5-6 mm) and <1 vol % amphibole (<2-3 mm). It is strongly iron carbonate-altered as illustrated by the iron-carbonate in the matrix and as veinlets (Fig. 9D), and by its high CO_2 content (7.37%) (Table 1). The normalized multi-element spider diagram shows characteristics similar to the syn-Timiskaming alkaline/shoshonitic to sub-alkaline intrusions (Fig. 6B). A recent update to the petrology of the upper Beaver intrusive complex is provided by Cloutier et al. (2023) who define the names of the various phases of the Upper Beaver intrusion based on their mineralogy and complementary lithogeohemistry.

Sample CH-919-14-DAT-01 was collected on the main mechanically stripped outcrop of the Cheechoo gold property, at the former helipad site, just above drill hole 1 (UTM NAD83 Zone 18, 438 657 m E, 5 830 276 m N: Figs. 2, 11). The intrusion, locally cut by sheeted veinlets and/or a stockwork of quartz (±feldspar) veins, is deformed, recrystallized, and foliated, as shown by elongated biotite and chlorite. The Cheechoo intrusion is the main host to the auriferous zones. The associated hydrothermal alteration mainly consists of decametric to metric Na-rich zones (early Au), centimetric K-Mg-rich replacement zones/bands (syn-Au) along V2 vein selvages, a more restricted calc-silicate assemblage (actinolite, diopside, and grossular) and traces of disseminated fine-grained arsenopyrite and pyrrhotite (Fontaine et al., 2018). A detailed description of the Cheechoo intrusion and its various facies is given in Fontaine et al. (2015, 2017, 2018). The sample is representative of the Cheechoo granodioritic-trondhjemitic dominant composition and consists of local feldspar phenocrysts in a homogeneous, very pale grey matrix of quartz, albite, microcline, biotite, and rare traces of diopside and actinolite (Fig. 9E, F). The selected sample is devoid of sulfides (<0.01 wt.% S) and paragneiss enclaves. It is siliceous, relatively fresh, and barren to very weakly anomalous with 25 ppb Au (Table 1). The selected sample plots in the rhyodacite field of Winchester and Floyd (1977) diagram (Fig. 5A) and in the granite field, close to the granodiorite field, in Middlemost (1994) TAS diagram (Fig. 5B). Its rare-earth elements pattern is flat, although alteration may have influenced the signature of this sample

(e.g., Ta: Fig. 6A, B). Representative, least-altered whole-rock geochemical composition of the Cheechoo intrusion is given in Fontaine et al. (2018).

ANALYTICAL WORK AND RESULTS

ID-TIMS U-Pb Zircon Geochronology Analytical Methods

Geochronology work presented here was done at the Jack Satterly Geochronology Laboratory (JSGL) at the University of Toronto for samples BFBD-2016-001, PLBD-2018-019, PLBD-2019-039, PLBD-2018-052, PLBD-2018-056, BDPL-KL-2018-202, and BDPL-KL-2018-201, whereas geochronology work for samples UB-07-157 and CH-919-14-DAT-01 was done at the Geochronology Laboratory at the Geological Survey of Canada.

Analytical Methods – Jack Satterly Geochronology Laboratory, University of Toronto

Rocks were initially crushed using a conventional jaw crusher, followed by grinding to a coarse powder using a hardened steel disk mill. Initial separation of heavy minerals was carried out by passing the heavy concentrate over a shaking, riffled water (Wilfley) table multiple times. Further processing employed density separations with methylene iodide and paramagnetic separations with a Frantz isodynamic separator. Final sample selection was achieved by hand picking in alcohol under a binocular microscope, choosing the freshest, least cracked, core-and inclusion-free grains of zircon. Analytical methods involved ID-TIMS following chemical abrasion (CA, modified after Mattinson, 2005). Zircon grains were annealed in quartz crucibles at 900°C for 2 days. This removes much, although not all, of the radiation damage induced by decay of U and Th contained in the mineral, rendering least altered zircon more inert to chemical attack. The annealed grains were subsequently leached in approximately 0.10 ml of concentrated hydrofluoric (HF) acid for up to several hours in Teflon vessels at 195°C. Altered parts of the crystals, which contain isotopically disturbed Pb, dissolve more rapidly than annealed, unaltered crystal domains for low to moderate levels of radiation damage. Attack is variable, depending on the uranium concentration of the grains and the consequent degree of radiation damage. Chemical abrasion has the advantage of penetrative removal of alteration domains where Pb-loss has occurred, and generally improves concordance. Weights of mineral fractions chosen for ID-TIMS analysis were estimated from scaled digital photomicrographs, using the density of zircon. Estimated weights should be accurate to about ±20%. This affects only U and Pb concentrations, not age information, which depends only on isotope ratio measurements (Table 2). Samples were washed briefly in 7N HNO_3 prior to dissolution. A mixed ^{205}Pb-^{235}U isotopic spike was added to the dissolution capsules during sample loading. Zircon grains were dissolved using concentrated HF in Teflon bombs at 195°C for 3-4 days, then dried and re-dissolved in 3N HCl overnight to promote total dissolution and full equilibration with the spike (Krogh, 1973). U and Pb were isolated using 50 microliter anion exchange columns using HCl elutions, dried down, and then loaded onto outgassed rhenium filaments with silica gel (Gerstenberger and Haase, 1997). Pb and UO_2 were analyzed on a VG354 mass spectrometer using a Daly collector in pulse counting mode. The mass discrimination correction for this detector was constant at 0.07%/AMU. Thermal mass discrimination corrections are 0.10%/AMU for Pb and U. Dead time of the Daly system was 18 ns for Pb during the analytical period, monitored using the SRM982 Pb standard. Mass spectrometer data was reduced using in-

house software (UtilAge program) coded by D. Davis at the University of Toronto. Corrections for initial ^{230}Th disequilibrium in zircon have been applied to the $^{206}Pb/^{238}U$ ages, assuming a Th/U ratio in the magma of 4.2. All common Pb was assigned to procedural blank. Initial Pb from geological sources above 1 picogram was corrected using the Pb evolution model of Stacey and Kramers (1975). Plotting of concordia curves and averaging of age results were carried out using the Isoplot 3.71 Add-In for MS Excel, of Ludwig (2009). The curve for Concordia is shown in some plots as a 'band', incorporating uncertainties in the ^{235}U and ^{238}U decay constants. Ages calculated are generally based on weighted averages of $^{207}Pb/^{206}Pb$ ages(ratios) or regressions using a modified version of the York (1969) algorithm, in which points are weighted proportional to the inverse of the square of the assigned errors, incorporating error correlations (see Ludwig, 2009); in cases involving secondary Pb loss chords, lower and upper Concordia intercept ages are provided, but do not incorporate uncertainties in the U decay constants. Probabilities of fit would be expected to be 50% on average for random data with correctly chosen analytical errors. All age errors and error ellipses are given at the 2 sigma or 95% level of confidence. Total common Pb levels in the analyzed zircon grains are frequently below 0.4 pg, but for some fractions reaches up to almost 6 pg, almost certainly due the presence of unavoidable mineral, melt, and/or fluid inclusions (see descriptions below), possibly related to the local effects of mineralizing fluids associated with these deposits. Typical procedural blanks in the JSGL lab are at the 0.2-0.4 pg level for Pb.

Analytical Methods – Geological Survey of Canada

Heavy minerals were concentrated using standard crushing, grinding, and separation on a Wilfley™ table and by heavy liquid techniques. Mineral separates were sorted by magnetic susceptibility using a Frantz™ isodynamic separator and hand-picked using a binocular microscope. All ID−TIMS analyses are of single zircon grains that were either air abraded (Krogh, 1982) or chemically abraded following the techniques of Mattinson (2005). The latter were annealed for 48 h at 1000°C prior to leaching with HF at 180°C for varying lengths of time. Details of zircon morphology, quality, and physical or chemical abrasion times are summarized in Table 3. ID-TIMS analytical methods, including addition of an in-house ^{205}Pb-^{233}U-^{235}U spike, dissolution, column chemistry, and analysis on a Triton thermal ionization mass spectrometer, are modified after Parrish et al. (1987). Treatment of analytical errors follows Roddick (1987). Mass fractionation of Pb was corrected using repeat analyses of NBS981 standard and amounted to 0.11 ± 0.0004 (1 S.D.)/a.m.u. Procedural blank levels were generally on the order of 0.9 to 2.8 pg for Pb. The isotopic ratios were corrected for the presence of initial common Pb above the laboratory blank using the Pb composition predicted by the model of Cumming and Richards (1975) for the date of the zircon fraction. Age calculations were done using a present-day $^{238}U/^{235}U$ ratio of 137.88 as recommended by Steiger and Jäger (1977) and decay constants of 1.55125×10^{-10} yr^{-1} and 9.8485×10^{-10} yr^{-1} for ^{238}U and ^{235}U, respectively, from Jaffey et al. (1971). The program ISOPLOT v. 4.15 (Ludwig, 2012) was used to generate concordia plots and derive ages. Corrected ratios are reported with 1σ analytical errors (68% confidence) in the data table and all age uncertainties and error ellipses are at the 95% confidence level in the concordia diagrams and in the text.

U-Pb Analytical Results

ID-TIMS results from the Jack Satterly Geochronology Laboratory and the Geochronology Laboratory at the Geological Survey of Canada are given in Tables 2 and 3, respectively. Transmitted light photomicrographs of representative best quality zircon grains, chosen for pre-treatment and for analysis, are shown in Figures 12–18. Most individual zircon grain fractions comprise chemically abraded single grains, but in one instance consisted of two tiny, narrow, elongate prismatic grains. U-Pb isotopic data for all zircon fractions from each individual sample are presented on conventional Concordia diagrams in Figures 12–18.

Sample BFBD-2016-001 (Black Fox): This sample yielded a relatively small number of zircons, but most grains present are of very good quality, dominantly colourless to very pale yellow, gemmy (well faceted and clear), short prismatic, or spindle forms. Best quality grains were <100 microns in maximum dimension. The resulting U-Pb data are highly consistent/reproducible and concordant (Fig. 12). Five single grain fractions cluster tightly on Concordia. Model $^{207}Pb/^{206}Pb$ dates range narrowly between 2702.1 to 2702.6 Ma (Table 2). Figure 12 shows a "Concordia Age" calculation (after Ludwig) - yielding 2702.3 ± 0.89 Ma (n = 5; excludes decay constant errors). The age quoted is identical to a weighted average $^{207}Pb/^{206}Pb$ age, or a regression of the data through the origin. Uranium concentrations were uniformly low (<75 ppm) and Th/U ratios consistent, between about 0.56–0.85. Although older than expected, 2702.3 ± 0.89 Ma is considered the crystallization age of the dyke, which is coeval with the Blake River Group (2704-2695 Ma: McNicoll et al., 2014) rocks hosting gold mineralization at the Black Fox mine.

Sample PLBD-2018-019 (Bachelor): A modest amount of zircon was recovered from this sample of the O'Brien intrusion, consisting principally of short (2:1) to elongate (up to 4 or 5:1) prismatic, square or slightly flat grains, pale brown to medium reddish-brown in colour, commonly with mineral and/or melt inclusions. Maximum grain size reaches ~200 microns. Several best-quality zircon grains were selected for analysis following annealing and etching pre-treatment. The resulting U-Pb data for six single grains are provided in Table 2 and shown graphically in Figure 13. Five of the fractions yield results that are highly colinear, ranging from 0.1-0.8% discordant, and give an upper intercept age of 2692.1 ± 2.0 Ma with excellent fit (97%) and is interpreted to represent the crystallization age of the O'Brien intrusion. A sixth fraction (Z4) is essentially concordant but has a slightly younger $^{207}Pb/^{206}Pb$ age of 2688.5 ± 1.4 Ma; the significance of this analysis is unclear – it could reflect minor ancient Pb-loss or reflect an analytical artefact, although the analysis, with only 0.29 pg total common Pb, is insensitive to uncertainties in a common Pb correction. The lower intercept of the regression, at 927 ± 460 Ma, defines a broadly Grenvillian isotopic disturbance.

Sample PLDB-2018-039 (Francoeur): This sample yielded no U-Pb datable accessory phases.

Sample PLDB-2018-052 (Thunder Creek – Timmins West complex): This sample yielded no U-Pb datable accessory phases.

Sample PLDB-2018-056 (HWY-144 – GAP deposit Timmins West complex): This sample yielded only a very sparse recovery of fine-grained zircon, having somewhat diverse morphologies (Fig. 14). Rounded forms occur, suggesting the presence of xenocrysts or inherited zircon from country

rocks. Most zircon grains are clouded, indicating significant post-emplacement alteration of radiation-damaged domains. Out of the best 18 grains picked from this syenite, only a few showed morphological characteristics suggestive of magmatic crystallization (e.g., "sharp" straight-edged short prismatic forms with local pyramidal terminations), but even these appear badly altered. Following annealing and short-duration etching in concentrated hydrofluoric acid (~2.5 h), most crystals had completely disintegrated. A few extremely small blocky, square fragments remained, and several were selected for complete digestion and U-Pb analysis. The isotopic result for one of these grains (Z1) was strongly discordant, furnished no useful information and is not reported here. However, Table 2 shows results for four subsequent fractions, which although characterized by a weak Pb signal intensity, yielded data that help constrain the age of the syenite porphyry. Fractions Z2, Z4, and Z5 have concordant or near-concordant $^{207}Pb/^{206}Pb$ ages between 2677.3 Ma and 2679.8 Ma; a weighted average $^{207}Pb/^{206}Pb$ age for these three analyses is 2679.7 ± 1.6 Ma (MSWD = 0.14, probability of fit = 87%; Fig. 14) and is interpreted as the crystallization age of the syenite hosting the HWY-144 (144 GAP) gold deposit. The relative imprecision of fraction Z5 resulted from a very weak signal due to low U and radiogenic daughter Pb. A fourth fraction, Z3, overlaps concordia but has a slightly older $^{207}Pb/^{206}Pb$ age (2686.4 Ma) and likely reflects minor inheritance.

Sample BDPL-KL-2018-202 (Macassa mine – Kirkland Lake deposit): A modest amount of zircon was recovered from this syenite porphyry sample. However, there is also a moderate degree of heterogeneity to the morphologies and sizes within the zircon population, suggesting that many grains may be in part xenocrystic (Fig. 15). A total of seven fractions, mostly single grains, have been chemically-abraded and analyzed from this sample, with results reported in Table 2. The concordia diagram in figure 15 illustrates how an older set of analyses (Z1, Z2) cluster concordantly at ca. 2699 Ma, though they are imprecise due to a combination of low U, resultingly low radiogenic Pb, and a high proportion of common Pb (exceeding the laboratory blank). Conceivably, alteration of these zircon grains has not been completely removed during the chemical abrasion pretreatment. Slightly younger analyses are represented by concordant fractions Z5 and Z7, having $^{207}Pb/^{206}Pb$ ages of 2692.3 ± 2.6 Ma and 2692.1 ± 4.0 Ma. The youngest identified zircon fractions in this "syenite" – Z3, a clear colourless tip; Z4, two elongate tiny prisms; and Z6, a clear, broken prism segment – yield consistent $^{207}Pb/^{206}Pb$ ages of 2686.6 ± 2.0 Ma, 2686.1 ± 20.9 Ma, and 2686.6 ± 2.1 Ma, respectively (Fig. 15). Reversely discordant analysis Z4, with a weak radiogenic Pb* signal, was affected by poor counts and a high proportion of common Pb. A weighted average age for the three youngest fractions is controlled by the most precise result for fraction Z3 and could suggest a maximum emplacement age of 2686.6 ± 1.4 Ma. Moreover, the morphological diversity of zircons, and the demonstrable presence of xenocryst populations in this sample warrant caution that the syenite porphyry described here is dominated by inheritance. Such an interpretation is supported by the fact that the 2686.6 ± 1.4 Ma age is older than the maximum age of the host Timiskaming sedimentary rocks intruded by the syenite porphyry in the Kirkland Lake area (2680 ± 3 Ma, Corfu et al., 1991). A more robust estimate for the age of the syenitic ore zone host at the Macassa 04 Break is likely furnished by the results for BDPL-KL-2018-201 (see below).

Sample BDPL-KL-2018-201 (Macassa mine – Kirkland Lake deposit): This least altered sample of the syenite porphyry yielded a modest recovery of zircon, characterized by somewhat diverse morphologies including larger, medium-brown (typically short) prisms, and at least one other subpopulation of smaller, more pale or colourless, straight-walled elongate prisms, in places

broken (Fig. 16). Analytical work was focused on the finer-grained population in the expectation of avoiding inherited components, though xenocrystic zircon was still found to be present: of seven total single grain fractions (all of which are ≤ 0.6% discordant), four initial analyses (Z1–Z4) proved to contain older Pb, with $^{207}Pb/^{206}Pb$ ages ranging from 2694.7 ± 2.6 Ma down to 2678.8 ± 1.8 Ma (Table 2). The remaining three fractions, all small, cloudy-etched broken elongate prisms (Z5–Z7) yielded consistent, reproducible, and concordant $^{207}Pb/^{206}Pb$ ages of 2677.0 ± 1.8 Ma, 2676.5 ± 1.6 Ma, and 2676.1 ± 2.9 Ma (Table 2, Fig. 16). A calculated weighted average $^{207}Pb/^{206}Pb$ age for these three analyses is 2676.6 ± 1.1 Ma (MSWD = 0.18; probability of fit = 84%). This new age is considered to be a robust estimate of the timing of emplacement and crystallization of the syenite porphyry hosting ore at the Macassa mine and the bulk of the gold in the giant Kirkland Lake deposit (Ispolatov et al., 2008; Dubé and Mercier-Langevin, 2020 and references therein).

Sample UB-07-157 (Upper Beaver): This sample contained clear to mildly turbid, pale brown, euhedral, stubby prismatic to prismatic zircon crystals with well-defined growth zoning (Fig. 17). Thirteen single zircon grains analyzed yield a spread of concordant to discordant (up to 5.9 %) $^{207}Pb/^{206}Pb$ dates between 2686 and 2674 Ma (Table 3; Fig. 17). Ten of the thirteen analyses lie on a regression line with an upper intercept at 2678.7 ± 0.7 Ma and a lower intercept at 175 ± 70 Ma (MSWD = 0.53; probability of fit = 0.83). Zircon grains A2, Z1B, and Z2A may have experienced a different Pb-loss pattern than the other analyses and (or), in the case of fractions A2 and Z2A, may contain a minor inherited component. The upper intercept age of 2678.7 ± 0.7 Ma is interpreted as the time of igneous crystallization of the post-ore "spotted porphyry" at Upper Beaver.

Sample CH-919-14-DAT-01 (Cheechoo): This sample of the Cheechoo intrusion yielded mostly clear to rarely turbid, colourless or brown, stubby prismatic to prismatic zircon crystals as well as subequant or anhedral grains (Fig. 18). Four out of six single-grain fractions yield a cluster of sub-concordant analyses (≤0.5% discordant) (Table 3; Fig. 18). Three of these analyses (A16-1, A16-3, and A16-4), consisting of brown subequant to prismatic crystals, give consistent $^{207}Pb/^{206}Pb$ dates of 2612.1 ± 1.5 Ma, 2612.4 ± 1.4 Ma, and 2612.3 ± 1.6 Ma, respectively. A weighted average $^{207}Pb/^{206}Pb$ age for these three analyses is 2612.3 ± 0.8 Ma (MSWD = 0.04; probability of fit = 0.96), interpreted to represent the crystallization age of the Cheechoo intrusion (Fig. 18). The fourth analysis in this cluster (B16-1), a brown anhedral fragment, yields a slightly younger $^{207}Pb/^{206}Pb$ date of 2610.0 ± 1.4 Ma. Inclusion of this analysis in a weighted mean age calculation gives a relatively high MSWD of 2.6, suggesting the presence of non-analytical scatter possibly owing to minor ancient Pb loss compared to the other three analyses. A colourless prism with rounded edges (A16-2) gives a distinctly older $^{207}Pb/^{206}Pb$ date of 2706.8 ± 1.8 Ma indicating inheritance. Zircon fraction A6-1, a turbid, brown stubby prism, yields a highly discordant (10.6%) $^{207}Pb/^{206}Pb$ date of 2498.0 ± 1.5 Ma, likely owing to strong alteration and (or) short-duration chemical abrasion (6 hours compared to 16 hours for all other fractions).

GENERAL CONSIDERATIONS AND CONSTRAINTS ON THE TIMING OF GOLD MINERALIZATION

The Superior Province hosts several major gold districts that share a number of common geological features, with recurring types and styles of gold deposits. The controls on the formation of these various types of gold deposits are generally relatively well understood, although the exact timing of gold introduction remains unclear in many cases. Field relationships combined with precise U-Pb geochronology remain the best elements in constraining the age of formation of a deposit, which allows one to associate ore-forming activity with specific geological events or features, helping refine exploration and genetic models. The ages on intrusive rocks spatially associated with gold deposits presented in this report help better constrain the timing of mineralization by providing a maximum age (when the dated intrusive rock hosts the mineralized zones), or a minimum age (when the dated rock cuts the mineralized zones). Such information may be useful especially for intrusion-associated deposits where the role played by intrusion, active or passive, in the formation of such deposits remains controversial (e.g., Robert, 2001; Dubé and Mercier-Langevin, 2020; Mathieu, 2021; Goldfarb and Pitcairn, 2023).

The 2702.3 ± 0.89 Ma deformed and mineralized intermediate dyke sampled at the Black Fox mine (sample BFBD-2016-001) is older than expected but may be an indication of early favourable structural ground preparation. The area east of Matheson is also characterized by the presence of pre- to syn-Timiskaming quartz-feldspar porphyries, alkaline to sub-alkaline intrusions and dykes of various compositions (e.g., the Garrison stock 2678 ± 2 Ma; Corfu et al., 1989), pervasive iron-carbonate alteration, stockwork-disseminated-replacement gold mineralization, and orogenic quartz-carbonate vein networks, as illustrated by the ore at the Black Fox mine, within or proximal to the Destor-Porcupine fault zone (Fig. 1). This, combined with the age of the dated dyke, indicates that this crustal-scale fault acted as major magmatic and hydrothermal conduits over a long period of time (Dubé and Mercier-Langevin, 2020 and references therein).

The 2692.1 ± 2.0 Ma upper intercept age for the porphyry intrusion at the Bachelor mine in the northern Abitibi belt (sample PLBD-2018-019) is interpreted to represent the best estimate of the timing of emplacement and crystallization of the O'Brien intrusion and the maximum age of the bulk of gold mineralization. The age is similar to that reported for the Lac Shortt carbonatite (2691 +5/-3 Ma; Joanisse, 1994), carbonatite from the lac Lacroix alkaline complex (2687.8 ± 2.8 Ma; Augland et al., 2015), as well as the Berthiaume syenite (2688 ± 1 Ma; Davis et al., 2005) in the northern Abitibi greenstone belt. A more accurate age for the lac Lacroix complex carbonatite is likely offered by its most concordant zircon fraction at 2693 ± 3 Ma (Augland et al., 2015, their Table 2). More recently, the Chevrillon pluton north of Chibougamau (Fig. 1) has been dated at 2693.1 ± 1.7 Ma (Huguet et al., 2018). The age for the O'Brien intrusion is distinctly older than those determined for the Douay syenite (2676 +6/-5 Ma: Davis et al., 2000) in northern Abitibi, or the Beattie syenite (2682.9 ± 1.1 Ma: David et al., 2007; 2681.6 ± 1.0 Ma: Mueller et al., 1996), and the Clericy syenite (2682 ± 3 Ma: Mortensen, 1993), as well as younger syenite, monzonite, and monzodiorite of the southern Abitibi belt (e.g. Dubé and Mercier-Langevin, 2020 and references therein). At Bachelor, mutual cross-cutting relationships between quartz-syenite, monzodiorite to granodiorite dykes, and the main ore zones are compatible with a magmatic hydrothermal system centered on the O'Brien intrusion (Buro, 1984; Lauzière, 1989; Fayol and Jébrak, 2017). However, as indicated in Dubé and Mercier-Langevin (2020), some of the ore at

Bachelor is controlled by ENE-oriented brittle-ductile structures that locally crosscut the O'Brien intrusion, suggesting not only intrusion-driven fractures and replacement zones as the intrusion was emplaced, but also a contribution from a post-magmatic, syn-deformation mineralizing event (WAC zone; see figure 8H in Dubé and Mercier-Langevin, 2020).

The 2679.7 ± 1.6 Ma crystallization age of the syenite hosting the HWY-144 (144 GAP) gold deposit (sample PLBD-2018-056) would be equivalent to the age of some of the older syn-Timiskaming syenitic bodies in the southern Abitibi belt, notably those adjacent to or within the Larder Lake-Cadillac fault zone (Fig. 1), such as the Otto Stock (2679 ± 1 Ma: Corfu and Noble, 1992), the Cairo stock (ca. 2676 Ma: Ayer et al., 2005; Berger, 2006), the Upper Beaver syenite (2679 ± 1 Ma: see below) and the Young-Davidson syenite (2679 ± 2 Ma: Zhang et al., 2011), or those nearer the Destor-Porcupine fault zone such as the alkaline Garrison stock (2678 ± 2 Ma: Corfu et al., 1989). More importantly the 2679.7 ± 1.6 Ma crystallization age represents the maximum age of gold mineralization at the HWY-144 (144 GAP) gold deposit and as such the Timmins West complex. At Timmins West, as well as the Young-Davidson and Matachewan gold deposits further to the south along the Larder Lake-Cadillac Fault zone, shallow to moderately dipping mm- to cm-thick gold-bearing quartz ±sulfides and/or quartz ±pyrite-carbonate veinlets-vein arrays present within the ore zones (Fig. 8E) are at high-angle to the moderately to steeply plunging L_3 stretching lineation indicating formation during the main phase of shortening (D_3) (Derry et al., 1948; Martin, 2012; Zhang et al., 2014; Campbell, 2014; Kallio and Vaz, 2016; Dubé and Mercier-Langevin, 2020). The passive role of the syn-Timiskaming syenite host intrusions is further supported by the presence of ore in carbonatized D_3 shear zones (e.g., Rusk and Holmer) at Timmins West, (Rhys, 2010; Kallio and Vaz, 2016, Dubé et al., 2020). The gold mineralization is arguably syn-D_3 main phase of shortening (Dubé and Mercier-Langevin, 2020; Dubé et al., 2020).

A CA-ID-TIMS U-Pb zircon age of 2676.6 ± 1.1 Ma for the least-altered Macassa syenite porphyry (sample BDPL-KL-2018-201) represents a significant improvement over previous attempts to precisely date the main ore host of the giant Kirkland Lake deposit. A previous study by Ispolatov et al. (2008) included an air abrasion ID-TIMS study of zircons from the syenite porphyry at Discovery outcrop on the Main Break. The youngest grain identified had a $^{207}Pb/^{206}Pb$ date of 2689.6 ± 4.7 Ma, which at the time was concluded to be an inherited component since the Timiskaming clastic rocks that host the syenite porphyry intrusion at Kirkland Lake were dated themselves to be younger than 2680 ± 3 Ma (youngest detrital zircon age: Corfu et al., 1991). A parallel SHRIMP ion probe dating study included in that work confirmed the dominance of inherited zircon in the syenite porphyry, though a single young spot analysis in the center of a heavily cracked zircon grain did reveal a $^{207}Pb/^{206}Pb$ age at 2674 ± 6 Ma (Ispolatov et al., 2008), within error of the age determined here. The vast majority of Abitibi "syenite" in the southern Abitibi belt have ages between 2683-2670 Ma, and one could conclude on this basis that even the youngest analyzed zircon (2686.6 ± 1.4 Ma) so far from the syenite porphyry BDPL-KL-2018-202 are xenocrystic in origin (a recognized issue with many syenite bodies). Strictly speaking, therefore, the ca. 2686.6 ± 1.4 Ma age described above for sample BDPL-KL-2018-202 should conservatively be regarded as a maximum age for the Macassa syenite porphyry at this location, whereas the 2676.6 ± 1.1 Ma obtained from sample BDPL-KL-2018-201 is more likely to be the age of crystallization of the syenite porphyry. Although, there are many felsic Abitibi intrusive bodies with crystallization ages between ca. 2690-2680 Ma (e.g., the 2688 ± 1 Ma Berthiaume

syenite in the northern Abitibi: Davis et al., 2005), most are pre-main shortening though they have been classified based on fabrics as being either syntectonic or post-tectonic (Chown et al., 1992, 2002; Mathieu, 2021). Additionally, while most of these ca. 2690-2690 Ma intrusions have TTG affinities and, are quartz-feldspar porphyries, fewer are truly alkaline or contain significant volumes of syenitic-shoshonitic rock compositions (Dubé and Mercier-Langevin, 2020).

The study by Ispolatov et al. (2008) also included Re-Os analyses of molybdenite from auriferous quartz veins sampled from mining stopes in the Macassa mine. Four analyzed samples consisted of auriferous quartz veins, with very fine-grained molybdenite occurring largely as coatings on slip surfaces and fractures. Due to the very fine grain size of molybdenite, mineral separates obtained were not completely pure. As indicated in Ispolatov et al. (2008), Re-Os model ages range from 2977 ± 8 Ma to 2666 ± 8 Ma but two fractions from their sample 4744 yielded internally consistent ages of 2677 ± 8 Ma and 2666 ± 8 Ma. This sample was further examined by preparing a full mineral separate. Ages of two fractions of this bulk separate, 2679 ± 8 Ma and 2678 ± 7 Ma, agree with each other and with the ages of the drilled concentrate (Ispolatov et al., 2008). The four analyses of sample 4744 yield a weighted average Re-Os age of 2675 ± 6 Ma. Only ages of sample 4744 are compatible with available geological constraints, i.e. are younger than the maximum depositional age of Timiskaming clastic rocks in the Kirkland Lake district area. All other results exceed the maximum age of Timiskaming rocks (2680 ± 3 Ma: Corfu et al., 1991; 2677.7 ± 3.1 Ma: Ispolatov et al., 2008) and thus cannot have any geological significance. The weighted mean age of 2675 ± 6 Ma suggests that the timing of mineralization may have closely overlapped the age of emplacement and crystallization of the 2676.6 ± 1.1 Ma syenite porphyry. However, considering the unexplained complexity of the other Re-Os results and the occurrence of an internally consistent but inaccurate date (2696 ± 7 Ma and 2694 ± 7 Ma: Tegren-Gracie sample), Ispolatov et al. (2008) conclude that the Re-Os age of sample 4744 cannot be interpreted as conclusive. The only age that would be compatible with the geological setting and field relationships is the youngest result from sample 4744: 2666 ± 8 Ma. The Kirkland Lake deposit (including the South Zone Complex) is controlled by reverse oblique brittle to brittle-ductile fault zones known as the Main Break (~400–450 m vertical displacement: Thomson, 1950), the 04 Break, and the Amalgamated Break to the south. The ore zones are structurally controlled by these faults and hosted by the syenite intrusive complex but also by the Timiskaming trachytic lava flow and more locally sedimentary rocks. The mineralization must thus be younger than: 1-the age of the syenite porphyry (2676.6 ± 1.1 Ma), 2-the maximum age of the Timiskaming sedimentary rocks in Kirkland Lake (2680 ± 3 Ma), and also the age of the trachyte (Timiskaming volcanic flow) from the Kirkland Lake district area dated at 2669.6 ± 1.4Ma (Ispolatov et al., 2008). Considering the strong structural control, the style of mineralization (quartz-carbonate veins, quartz-breccias veins, cataclasite and replacement ore), the age or maximum age of the host rocks and the inconclusive results of the Re-Os dating, gold mineralization within the Kirkland Lake deposit needs to be post-Timiskaming and most probably within the ca. 2660–2640 ± 10 Ma range as proposed by Dubé and Mercier-Langevin (2020). The epizonal nature of the deposit as illustrated by the host brittle to brittle-ductile structures may be explained by the shallower crustal level of the geological setting evidenced by the unusually thick succession (3–5 km) of Timiskaming conglomerate, sandstone and local sub-aerial alkaline volcanic and volcaniclastic rocks that extends for nearly 60 km in the Kirkland Lake area north of the Larder Lake-Cadillac fault zone (e.g., Dubé and Mercier-Langevin, 2020 and references therein).

The Kirkland Lake deposit shares strong analogies with epithermal deposits related to alkaline magmatism as defined by Jensen and Barton (2000), including alkaline/sub-alkaline intrusive hosts, a strong correlation between Au and Te, and the overall style of high-grade (low base metal) mineralization, and alteration (Ispolatov et al., 2008). However, the hydrothermal fluids cannot be derived from the exposed alkaline-subalkaline intrusive complex which is crosscut and displaced by the gold-bearing Main Break, 04 Break, and Amalgamated Break faults network. Additionally, if the fluids originated from a deeper magmatic source, the parent magmatic phase(s) remains to be identified (Ispolatov et al., 2008). The gold- and telluride-bearing quartz veins and breccias in the Kirkland Lake deposit are hosted in structures that are more compatible with D_3 reverse-oblique faults (Dubé and Mercier-Langevin, 2020). Ispolatov et al. (2008) proposed that gold- and telluride-bearing quartz veins of the Kirkland Lake deposit were emplaced during D_4, synchronous with reverse-dextral movement along the ore-controlling brittle Kirkland Lake fault. In this case, the mineralization could not be related to syn-Timiskaming magmatism as three generations of fabrics formed during post-Timiskaming regional deformation (D_2, D_3, and D_4, local terminology) of the belt.

The Upper Beaver Au-Cu (± Mo) deposit is in the southernmost part of the 2704–2695 Ma (Ayer et al., 2002; McNicoll et al., 2014) western Blake River Group (formerly known as Kinojevis in that area; Roberts and Morris, 1982). The deposit is approximately 5–6 km north of the Larder Lake-Cadillac fault zone (Fig. 1). It is spatially associated and partly hosted in dykes and apophyses of the Upper Beaver intrusive complex (Roberts and Morris, 1982). The Upper Beaver intrusive complex consists of a mixed suite of mafic and felsic rocks of sub-alkaline (calc-alkaline) to alkaline affinity that includes variably hornblende phyric dioritic, monzodioritic, and quartz-monzodioritic rocks, plagioclase phyric rocks and rare quartz-feldspar phyric dykes (Kontak et al., 2008; Feick, 2016; Dubé and Mercier-Langevin, 2020; Cloutier et al., 2023). Multiple phases of alteration and mineralization occur which includes an early Au(-Cu) event hosted in a stratabound skarnoid type alteration (i.e., sodic-calcic assemblages ± magnetite/hematite), and later crosscutting sheeted quartz-molybdenite veins (Mercier-Langevin et al., 2021; Sutton et al., 2023), but the main Au(-Cu) event is associated with steeply dipping quartz-dominant veins, also characterized locally by abundant ± magnetite/hematite±chalcopyrite, that crosscut the aforementioned features and is instead spatially associated with a swarm of plagioclase phyric rocks (the ‘crowded porphyry unit). The “spotted porphyry” unit (plagioclase- and amphibole-bearing diorite) is the youngest intrusive phase, as shown by cross-cutting relationships (Roberts and Morris, 1982; Kontak et al., 2008, 2013; Feick, 2016; Cloutier et al., 2023). That all units of the intrusive suite plus the altered and mineralized sections are variably foliated indicates that mineralization was formed prior to the main regional shortening and coeval with the emplacement of the intrusive complex (Kontak et al., 2011, 2013). The crystallization age of the spotted porphyry presented here (sample UB-07-157: 2678.7 ± 0.7 Ma) thus provides a minimum age for the mineralization, as previously indicated in Kontak et al. (2011, 2013), Dubé and Mercier-Langevin (2020), and Mercier-Langevin et al. (2021). This is in agreement with a molybdenite Re-Os age of ca. 2685 Ma that was obtained from a gold-rich sericite-altered zone associated in the intrusive complex (Kontak et al., 2013) and a 2680.5 ± 5.9 Ma molybdenite Re-Os age from a quartz-carbonate vein that clearly shows the direct association between gold and molybdenite (Mercier-Langevin et al., 2021). These ages correspond to the timing of the early- to syn-Timiskaming intrusive rocks that are common along the major E-W fault zones of the southern Abitibi and makes the deposit part of the syn-Timiskaming intrusion-associated stockwork-disseminated, veinlet and replacement-style deposits (Dubé and Mercier-Langevin, 2020). The strong iron-carbonate alteration recorded by the post-ore “spotted porphyry” dyke (Table 1; Fig.

9D), in addition to the local presence of late crosscutting quartz-tourmaline-carbonate veins, is most probably the manifestation of the younger syn-orogenic style of alteration typical of many quartz-carbonate (± tourmaline) orogenic deposits along the Larder Lake-Cadillac Fault zone to the south and illustrates the time gap between the early- to syn-Timiskaming intrusion-associated stockwork-disseminated (ca. 2683–2670 Ma) and the orogenic gold systems in southern Abitibi (2660-2640 ±10 Ma: Dubé and Mercier-Langevin, 2020).

The Cheechoo intrusion is emplaced within the transitional zone between the Opinaca Subprovince to the north and the La Grande Subprovince to the south (Fig. 2). The area is characterized by a strong metamorphic gradient illustrated by paragneiss and migmatite, syn- to late-tectonic intrusions, leucogranitic pegmatite, conglomerate, local iron-rich formation, and amphibolite (Bandyayera et al., 2010; Morfin et al., 2013; Fontaine et al., 2017, 2018). The high-precision 2612.3 ± 0.8 Ma Cheechoo intrusion (sample CH919-14-DAT-01) hosts the bulk of the gold mineralization at the Cheechoo prospect and was emplaced in paragneiss, including the <2714 Ma (basal conglomerate), <2697 Ma (middle turbiditic subdivision), and <2675 Ma (upper greywacke) Low Formation of the La Grande Subprovince (Ravenelle et al., 2010; Ravenelle, 2013; Fontaine et al., 2018), probably early during the main phase of deformation (D_2) and amphibolite-facies metamorphism. This is supported by the presence of S_2 and S_3 metamorphic foliations and the saccharoidal texture of the Cheechoo intrusion matrix and gold-bearing veins. The strongly foliated domains near intrusion margins are associated with numerous leucogranitic pegmatite bodies. The intrusion is affected by late- to post-emplacement high-strain zones and folds related to the late-D_2 to D_3 deformation (Fontaine et al., 2018; Fontaine, 2019).

The high-precision ID-TIMS crystallisation age of the Cheechoo intrusion clearly indicates that the maximum age of the bulk of gold mineralization of the Cheechoo gold property is 2612 Ma. This age is penecontemporaneous with the 2618 ± 2 Ma Vieux Comptoir suite consisting of syn- to late-tectonic intrusions present in the La Grande, Opinaca and Opatica subprovinces and characterized by a pegmatitic texture, a granitic composition and the presence of biotite, muscovite, tourmaline and garnet (David and Parent, 1997; Goutier et al., 1999; Goutier, 2017; Fontaine et al., 2018). Furthermore, a pegmatitic granite from the Vieux Comptoir suite yielded a U-Pb crystallisation age of 2613.61 ± 0.44 Ma at the Orfée gold prospect (Bogatu and Huot, 2016). The 2612.3 ± 0.8 Ma age of the Cheechoo intrusion also corresponds to the emplacement of syn- to late-tectonic intrusions and pegmatite dykes in the La Grande Subprovince along the contact with the Opinaca Subprovince, especially in the vicinity of the Éléonore gold mine where pegmatites (some of which are mineralized) have been dated at 2620-2603 Ma (Ravenelle et al., 2010; Dubé et al., 2011; Dubé, 2017; Fontaine et al., 2015). The mapping and structural analysis of the two main "trenches" by Fontaine et al. (2018) indicates the auriferous vein network is pre-peak metamorphism and developed late during D_2, near the margins of the Cheechoo intrusion, in spatial association with pegmatite dykes. De Souza et al. (2023) similarly indicate that mineralization is pre-peak metamorphism, which they dated at 2609 Ma (LA-ICPMS U-Pb on monazite). However, de Souza et al. (2023) consider that mineralization at Cheechoo may be older and perhaps pre- to early-D_2 based on a preliminary ca. 2640 Ma LA-ICP-MS U-Pb zircon age for the intrusion. They therefore bracket the hydrothermal and auriferous activity between 2640 and 2609 Ma, a protractive period that coincides with pegmatite emplacement and prograde metamorphism in the region (Dubé et al., 2011, 2017, Fontaine et al., 2017). Fontaine et al. (2018) consider that the style and nature of auriferous mineralization and associated alteration, combined with the composition of the host reduced intrusion, share analogies with reduced intrusion-related

gold systems in which gold mineralization occurred during long-lived tectonometamorphic event(s) intimately associated with the emplacement of the Cheechoo reduced intrusion and a swarm of leucogranitic pegmatite dykes within metasedimentary rocks near a Subprovince boundary, which are common features of Archean gold mineralization in metamorphosed and deformed terranes (Goldfarb et al., 2005). More importantly, gold mineralization hosted by the 2612 Ma Cheechoo intrusion is a new style of gold mineralization in the Éléonore gold mine area and elsewhere in the Eeyou Istchee James Bay region and the age and composition of the intrusion may represent a new regional metallotect (Fontaine et al., 2018).

CONCLUDING REMARKS

This report, which is purposefully brief, presents key, high-precision U-Pb zircon ages on a series of intrusive rocks bodies that are spatially associated with Neoarchean gold deposits of the Superior Province (Abitibi greenstone belt and La Grande subprovince). These ages, which have been previously reported in various reports and oral and poster presentations but were never formally published, provide further constraints on the timing of gold mineralization in both emerging and mature mining camps. More specifically, these ages help clarify the relationship between major gold ore-forming events and specific magmatic and tectonometamorphic events related to the evolution of the Abitibi greenstone belt and La Grande subprovince.

ACKNOWLEDGMENTS

This study, although initiated during phase 3 of the Targeted Geoscience Initiative (2005-2010) *Abitibi Project* and continued through phases 4 (2010-2015: *Lode Gold Project*) and 5 (2015-2020: *Gold Project*), represents a contribution to the current "*OS-3 – Orogenic gold deposits: A closer look at the diversity of types, styles and ages of gold deposits in greenstone belts*" project of the Targeted Geoscience Initiative Program phase 6 (2020-2025). The authors are most grateful to Agnico Eagle Mines, Bonterra Resources, Globex Mining, Kirkland Lake Gold, McEwen Mining, Pan American Silver, Primero Mining, Queenston Mining, and Sirios Resources, for access to samples and data, and for scientific support. Thanks to C. Adams, E. Alexander, C. Beausoleil, C. Blanchette, W. Bleeker, T. Brace, T. Brisson, S. Carmichael, O. Côté-Mantha, D. Doucet, J. Dubé, S. Farrell, J. Gauthier, M. Gauthier, J. Goutier, K. Green, E. Kallio, F. Lefebvre, J-M. Lulin, H. Poulsen, D. Rhys, P. Riopel, F. Robert, J. Sutton, and J. Turcotte for insightful discussions on the geology and gold metallogeny of the Abitibi greenstone belt and the Eeyou Istchee James Bay region. The staff of the ID-TIMS Geochronology Laboratory at the Geological Survey of Canada (J. Peressini, L. Cataldo, and C. Lafontaine) are thanked for their excellent work in generating the high-precision U–Pb ID–TIMS data for samples UB-07-157 and CH919-14-DAT-01. M. Boutin contributed to drafting some of the figures. Thanks to D. Coutts for his constructive review of an earlier version of the manuscript.

REFERENCES

Augland, L.E., David, J., Pilote, P., Leclerc, F., Goutier, J., Hammouche, H., Lafrance, I., Talla Takam, F., Deschênes, P.-L., et Guemache, M., 2015, Datations U-Pb dans les provinces de Churchill et du Supérieur effectuées au GEOTOP en 2012-2013: Ministère des Ressources naturelles et de la Faune, Quebec, RP 2015-01, 20 p.

Ayer, J.A., Amelin, Y., Corfu, F., Kamo, S., Ketchum, J., Kwok, K., and Trowell, N., 2002, Evolution of the southern Abitibi greenstone belt based on U-Pb geochronology: Authochtonous volcanic construction followed by plutonism, regional deformation and sedimentation: Precambrian Research, v. 115, p. 63–95.

Ayer, J.A., Thurston, P.C., Bateman, R., Dubé, B., Gibson, H.L., Hamilton, M.A., Hathway, B., Hocker, S.M., Houlé, M.G., Hudak, G., Ispolatov, V.O., Lafrance, B., Lesher, C.M., MacDonald, P.J., Péloquin, A.S., Piercey, S.J., Reed, L.E., and Thompson, P.H., 2005, Overview of results from the Greenstone Architecture Project: Discover Abitibi Initiative: Ontario Geological Survey, Open File Report 6154, 146 p.

Bandyayera, D., Rhéaume, P., Maurice, C., Bédard, E., Morfin, S., and Sawyer, E., 2010, Synthèse géologique du secteur du reservoir Opinaca, Baie James: Ministère des Ressources naturelles et des Forêts, RG 2010-02, 46 p.

Berger, B.R., 2006, Geological synthesis along Highway 66 from Matachewan to Swastika: Ontario Geological Survey, Open File Report 6177, 125 p.

Bogatu, A., and Huot, F., 2016, Minéralisation aurifère du gîte Orfée, Eeyou Istchee Baie-James, Québec: Ministère des Ressources naturelles et des Forêts, MB 2016-10, 47 p.

Brisson, H., 2014, Technical report on the mineral eesource and mineral reserve estimates for the Black Fox complex: Unpublished report addressed to Primero Mining Corporation. 214 p.

Buro, Y., 1984, Geology of the Bachelor Lake gold mine, Desmaraiville, Abitibi-Est, Quebec: Canadian Institute of Mining, Metallurgy and Petroleum Special Volume 34, p. 385-392.

Campbell, R., 2014, Controls on syenite-hosted gold mineralization in the western Timmins camp: Unpublished MSc thesis, University of Western Ontario, London, Canada, 143 p.

Chown, E.H., Harrap, R., and Moukhsil, A., 2002, The role of granitic intrusions in the evolution of the Abitibi belt, Canada: Precambrian Research, v. 115, p. 291-310.

Chown, E.H., Daigneault, R., Mueller, W., and Mortensen, J.K., 1992, Tectonic evolution of the Northern Volcanic Zone, Abitibi belt, Quebec: Canadian Journal of Earth Sciences, v. 29, p. 2211-2225.

Cloutier, M., Rottier, B., Sherlock, R., Beaudoin, G., Sutton, J., Cote-Mantha, O., Davies, J., Perrot, M., 2023, Magmatic evolution of the Archean Upper Beaver Intrusive Complex and its implications for Au-Cu mineralization: Proceedings of the 17th SGA Biennial Meetings 28 August – 1 September 2023, Zurich, Switzerland, v. 1, p. 24-27.

Corfu, F. and Noble, S.R., 1992, Genesis of the southern Abitibi greenstone belt, Superior Province, Canada: Evidence from zircon Hf isotope analyses using a single filament technique: Geochimica et Cosmochimica Acta, v. 56, p. 2081–2097.

Corfu, F., Krogh, T.K., Kwok, Y.Y., and Jensen, L.S., 1989, U–Pb zircon geochronology in the southwestern Abitibi greenstone belt, Superior Province: Canadian Journal of Earth Sciences, v. 26, p. 1747–1763.

Corfu, F., Jackson, S.J. and Sutcliffe, R.H. 1991. U-Pb ages and tectonic significance of late Archean alkalic magmatism and nonmarine sedimentation: Timiskaming Group, southern Abitibi belt, Ontario: Canadian Journal of Earth Sciences, v.28, p.489-503.

Couture, J.-F., and Pilote, P., 1993, The geology and alteration patterns of a disseminated, shear zone-hosted mesothermal gold deposit; the Francoeur 3 Deposit, Rouyn-Noranda, Quebec: Economic Geology, v. 88, p. 1664–1684.

Cumming, G.L., and Richards, J.R., 1975, Ore lead isotope ratios in a continuously changing Earth: Earth and Planetary Science Letters, v. 28, p. 155–171.

David, J., and Parent, M., 1997, Géochronologie U-Pb du Projet Moyen-nord : Ministère des Ressources naturelles et des Forêts, GM59903, 88 p.

David, J., Davis, D.W., Dion, C., Goutier, J., Legault, M., et Roy, P., 2007, Datations U-Pb effectuées dans la sous-province de l'Abitibi en 2005-2006: Ministère des Ressources naturelles et de la Faune, Quebec, RP 2007-01, 17 p.

Davis, W.J., Lacroix, S., Gariépy, C., and Machado, N., 2000. Geochronology and radiogenic isotope geochemistry of plutonic rocks from the central Abitibi subprovince: Significance to the internal subdivision and plutono-tectonic evolution of the Abitibi belt: Canadian Journal of Earth Sciences, v. 37, p. 117–133.

Davis, D.W., David, J., Dion, C., Goutier, J., Bandyayera, D., Rheaume, P. Roy, P., 2005, Datations U-Pb effectuées en support aux travaux de cartographie geologique et de compilation geoscientifique du SGNO (2003-2004): Ministère des Ressources naturelles et de la Faune, Quebec, RP 2005-02, 20 p.

Derry, D.R., Hopper, C.H., and McGowan, H.S., 1948. Matachewan Consolidated Mine: Canadian Institute of Mining and Metallurgy, Jubilee Volume, p. 638-643.

De Souza, S., Perrot, M., Turlin, F., Groulier, P.-A., Jébrak, M., and Turcotte, J., 2023. Gold mineralization and remobilization in metamorphosed and polydeformed Archean rocks of the Superior Province, Québec: insights from the Cheechoo deposit and its auriferous pegmatites: 6th International Archean Symposium – abstracts: Geological Survey of Western Australia, Record 2023/8, p. 168.

Dubé, B., 2017. Le gisement aurifère Éléonore, Eeyou Istchee Baie-James, Province du Supérieur: un système hydrothermal fertile et complexe dans un environnement hypozonal: Québec Mines 2017, Résumé des Conférences et des Photoprésentations, DV 2017-03, p. 41.

Dubé, B., and Mercier-Langevin, P., 2015, Targeted Geoscience Initiative 4: Contributions to the understanding of Precambrian lode gold deposits and implications for exploration: Geological Survey of Canada Open File 7852, 293 p.

Dubé, B., and Mercier-Langevin, P., 2020, Gold deposits of the Archean Abitibi greenstone belt, Canada: Society of Economic Geologists Special Publication 23, p. 669–708.

Dubé, B., Mercier-Langevin, P., Ayer, J., Pilote, J-L, and Monecke, T., 2020, Gold deposits of the world-class Timmins-Porcupine camp, Abitibi greenstone belt, Canada: Society of Economic Geologists Special Publication 23, p. 53–80.

Dubé, B., Ravenelle, J-F., McNicoll, V., Malo, M., Creaser, R., Nadeau, L., and Simoneau, J., 2011. The world-class Roberto gold deposit, Éléonore property, James Bay area, Superior province, Quebec: Insights from geology and geochronology: GAC-MAC-SEG-SGA Annual Meeting, Ottawa, 25-27 May, Abstracts Volume 34, p. 55.

Fayol, N., and Jébrak, M., 2017, Archean sanukitoid gold porphyry deposits: A new understanding and genetic model from the Lac Bachelor gold deposit, Abitibi, Canada: Economic Geology, v. 112, p. 1913–1936.

Feick, K.E., 2016, An evaluation of the lithologies and geochemistry of the Upper Beaver deposit of the Kirkland Lake area: Unpublished M.Sc. thesis, University of Western Ontario, Kinston, Ontario, Canada, 247 p.

Fontaine, A., Dubé, B., Malo, M., McNicoll, V., Brisson, T., Doucet, D., and Goutier, J., 2015, Geology of the metamorphosed Roberto gold deposit (Éléonore mine), Baie-James region, Québec: diversity of mineralization styles in a polyphase tectono-metamorphic setting: Geological Survey of Canada, Open File 7852, p. 209-225.

Fontaine, A., Dubé, B., Malo, M., Ravenelle, J.-F., Fournier, E., McNicoll, V., Beausoleil, C., Prud'homme, N., and Goutier, J., 2017, The Éléonore gold mine: Exploration, discovery and understanding of an emerging gold district in Eeyou Istchee James Bay, Superior Province, northern Québec, Canada: Proceedings of Exploration 17: Sixth Decennial International Conference on Mineral Exploration, p. 601–617.

Fontaine, A., Dubé, B., Malo, M., Turcotte, J., and Doucet, D., 2018. Geology of the Cheechoo gold property, Eeyou Istchee Baie-James, Superior Province, northern Quebec; Geological Survey of Canada, Open File 8403, 25 p.

Fontaine, A., 2019. Géologie des minéralisations aurifères de la mine Éléonore, Eeyou Istchee Baie-James, province du Supérieur, Québec, Canada: Unpublished Ph.D. thesis, Université du Québec, Institut national de la recherche scientifique, Québec, Canada, 526 p.

Gerstenberger, H., and Haase, G., 1997, A highly effective emitter substance for mass spectrometric Pb isotope ratio determinations: Chemical Geology, v. 136, p. 309–312.

Goldfarb, R.J., Baker, T., Dubé, B., Groves, D.I., Hart, C.J.R., and Gosselin, P., 2005, Distribution, character, and genesis of gold deposits in metamorphic terranes: Economic Geology 100th Anniversary volume, p. 407-450.

Goldfarb, R., and Pitcairn, I., 2023, Orogenic gold: is a genetic association with magmatism realistic?: Mineralium Deposita, v. 58, p. 5–35.

Goutier, J., 2017, Géologie de la région du lac Ewart, sous-provinces de La Grande et d'Opinaca, à l'est de Radisson, Municipalité Eeyou Istchee Baie-James, Québec, Canada : http://gq.mines.gouv.qc.ca/bulletins-geologiques/lac-ewart/.

Goutier, J., Dion, C., Lafrance, I., David, J., Parent, M., and Dion, C., 1999, Géologie de la région des lacs Langelier et Threefold (SNRC 33F/03 et 33F/04): Ministère des Ressources naturelles, RG 98-18.

Hicks, K.D., 1990, Magmatic-hydrothermal and wall rock alteration at the Lake Shore gold deposit, Kirkland Lake, Ontario: Unpublished MSc. thesis, University of Ottawa, 195 p.

Huguet, J., Mathieu, L., Bédard, L.P., and Hamilton, M., 2018, Pluton de Chevrillon: homogénéité et relation à la déformation: Québec Mines + Énergie Annual Meeting, Québec City, November 19-22, 2018, DV 2018-03, p. 55.

Ispolatov, V., Lafrance, B., Dubé, B., Creaser, R., and Hamilton, M., 2008, Geologic and structural setting of gold mineralization in the Kirkland Lake-Larder Lake gold belt, Ontario: Economic Geology, v. 103, p. 1309–1340.

Jaffey, A.H., Flynn, K.F., Glendenin, L.E., Bentley, W.C., and Essling, A.M., 1971, Precision measurement of half-lives and specific activities of ^{235}U and ^{238}U: Physical Review C, v. 4, p. 1889–1906.

Jensen, E.P., and Barton, M.D., 2000, Gold deposits related to alkaline magmatism: Reviews in Economic Geology 13, p. 279–314.

Joanisse, A., 1994, Datation de la carbonatite du lac Shortt. Université du Québec à Montréal, Département des Sciences de la Terre; document inédit, activité de synthèse, 16 p.

Kallio, E., and Vaz, N., 2016, 43-101 Technical Report, updated mineral reserve estimate for Timmins West mine and initial resource estimate for the 144 Gap deposit, Timmins, Ontario, Canada. Prepared for Lake Shore Gold Corp: Unpublished, 347p.

Kelly, C.H., 2021, Characterization of alteration and mineralization at the Archean Grey Fox and Hislop magmatic-hydrothermal gold deposits, Matheson, Ontario: Unpublished MSc thesis, Laurentian University, Sudbury, Ontario, Canada, 134 p.

Kontak, D., Dubé, B., and Benham, W., 2008, The Upper Beaver project, Kirkland Lake area: Investigation of a syenite-associated copper-gold deposit with magnetite-epidote-feldspar alteration: Ontario Geological Survey, Open File Report 6226, p. 12-1 to 12-12

Kontak, D.J., Dubé, B., and Kyser, T.K., 2011, Geological, petrological and geochemical observations of an Archean syenite-associated Cu-Au deposit, Kirkland Lake, Ontario: a temporal or genetic relationship: GAC-MAC-SEG-SGA Joint Annual Meeting, Abstracts Volume 34, p. 111.

Kontak, D., Dubé, B., McNicoll, V., Creaser, R., and Kyser, K., 2013, The Upper Beaver Au-Cu deposit, Kirkland Lake, Ontario, Canada: An Archean IOCG analogue or just an intrusion-related iron oxide copper-gold deposit? [abs.]: Geological Association of Canada-Mineralogical Association of Canada (GAC-MAC) Annual Joint Meeting, Winnipeg, May 22–24, 2013, Abstract Volume 36, p. 122.

Krogh, T.E., 1973, A low contamination method for hydrothermal decomposition of zircon and extraction of U and Pb for isotopic age determinations: Geochimica et Cosmochimica Acta, v. 37, p. 485–494.

Krogh, T.E., 1982, Improved accuracy of U-Pb zircon ages by the creation of more concordant systems using an air abrasion technique: Geochimica et Cosmochimica Acta, v. 46, p. 637−649.

Lauzière, K., 1989, Environnement géologique et minéralisation aurifère à la mine Batchelor, Desmaraisville, Québec: Unpublished MSc thesis, Université du Québec à Chicoutimi, Chicoutimi, Canada, 164 p.

Ludwig, K.R., 2009, User's manual for Isoplot 3.71 a geochronological toolkit for Excel: Berkeley Geochronological Center Special Publication 4, 72 p.

Ludwig, K.R., 2012, Isoplot 3.75, A geochronological toolkit for Microsoft Excel: Berkeley Geochronology Center Special Publication 5, 75 p.

Martin, R.D. 2012. Syenite-hosted gold mineralization and hydrothermal alteration at the Young-Davidson deposit, Matachewan, Ontario: Unpublished M.Sc. thesis, Ontario, Canada, University of Waterloo, 188 p.

Mathieu, L., 2021. Intrusion-associated gold systems and multistage metallogenic processes in the Neoarchean Abitibi greenstone belt: Minerals, 2012, 11, paper 261.

Mattinson, J., 2005, Zircon U-Pb chemical abrasion (CA-TIMS) method: Combined annealing and multi-step partial dissolution analysis for improved precision and accuracy of zircon ages: Chemical Geology, v. 220, p. 47–66.

McDonough, W.F., and Sun, S.S., 1995. The composition of the Earth: Chemical Geology, v. 120, p. 223-253.

McNicoll, V., Goutier, J., Dubé, B., Mercier-Langevin, P., Ross, P.-S., Dion, C., Monecke, T., Legault, M., Percival, J., and Gibson, H., 2014, U-Pb geochronology of the Blake River Group, Abitibi greenstone belt, Quebec, and implications for base metal exploration: Economic Geology, v. 109, p. 27–59.

Mercier-Langevin, P., Lawley, C.J.M., Castonguay, S., Dubé, B., Bleeker, W., Pinet, N., Bécu, V., Pilote, J.-L., Jackson, S.E., Wodicka, N., Honsberger, I.W., Davis, W.J., Petts, D.C., Yang, Z., Jautzy, J., and Lauzière, K., 2020, Targeted Geoscience Initiative 5, Gold Project: A summary of contributions to the understanding of Canadian gold systems, In: Targeted Geoscience Initiative 5: Contributions to the understanding of gold deposit, (ed.) P. Mercier-Langevin, C.J.M. Lawley, and S. Castonguay; Geological Survey of Canada, Open File 8712, p. 1–30.

Mercier-Langevin, P., Creaser, R.A., Dubé, B., Dubé, J., Kontak, D.J., Sutton, J., and Côté-Mantha, O., 2021, Molybdenite Re-Os ages of a gold-rich vein, Porphyry zone, Upper Beaver deposit, Abitibi greenstone belt, Ontario: Geological Survey of Canada, Open File 8789, 13 p.

Mercier-Langevin, P., Dubé, B., Houlé, M.G., Bécu, V., Sappin, A.-A., Pilote, J.-L., and Castonguay, S., 2022, Métallogénie de la ceinture de roches vertes de l'Abitibi, Canada: In S. Decrée (ed.), Ressources Métalliques 2 Cadre Géodynamique et Exemples Remarquables dans le Monde, Série Sciences – Géosciences – Ressources Naturelles : la Recherche Fondamentale Appliquée, ISTE Éditions, Londres, p. 61–134.

Mercier-Langevin, P., Dubé, B., Houlé, M.G., Bécu, V., Sappin, A.-A., Pilote, J.-L., and Castonguay, S., 2023, Metallogeny of the Abitibi greesntone belt, Canada: In S. Decrée (ed.), Metallic Resources 2 Geodynamic Settings and Remarkable Examples of the World, Sciences – Geosciences – Natural Resources Series: Applied Fundamental Research, ISTE Editions, London, In press.

Middlemost, E.A.K., 1994, Naming materials in the magma/igneous rock system: Earth-Sciences Reviews, v. 37, p. 215–224.

Morfin, S., Sawyer, E.W., and Bandyayera, D., 2013, Lage volumes of anatectic melt retained in granulite facies migmatites: An injection complex in northern Quebec: Lithos 169, p. 200–218.

Mortensen, J. K., 1993, U-Pb geochronology of the eastern Abitibi Suprovince. Part 2: Noranda-Kirkland Lake area: Canadian Journal of Earth Sciences, v. 30, p. 29–41.

Mueller, W.U., Daigneault, R., Mortensen, J.K., and Chown, E.H., 1996, Archean terrane docking: upper crust collision tectonics, Abitibi greenstone belt, Quebec, Canada: Tectonophysics, v. 265, p.127–150.

Parrish, R.R., Roddick, J.C., Loveridge, W.D., and Sullivan, R.W., 1987, Uranium-lead analytical techniques at the Geochronology Laboratory, Geological Survey of Canada: Radiogenic age and isotopic studies, Report 1, Geological Survey of Canada Paper 87-2, p. 3–7.

Pearce, J.A., 2008. Geochemical fingerprinting of oceanic basalts with applications to ophiolite classification and the search for Archean oceanic crust: Lithos, v. 100, p. 14-48.

Ravenelle, J.-F., Dubé, B., Malo, M., McNicoll, V., Nadeau, L., and Simoneau, J., 2010, Insights on the geology of the world-class Roberto gold deposit, Éléonore property, James Bay area, Quebec: Geological Survey of Canada, Current Research 2010-1, 26 p.

Ravenelle, J.-F., 2013, Amphibolite facies gold mineralization: an exemple from the Roberto deposit, Eleonore property, James Bay, Quebec: Unpublished Ph.D. thesis, Université du Québec, Institut national de la recherche scientifique, Québec, Canada 325 p.

Rhys, D. 2010. Structural study of gold mineralization in portions of the Timmins mine and Thunder Creek projects, Porcupine mining district, Ontario: Timmins, Ontario Internal Lake Shore Gold Corp Report.

Robert, F., 2001. Syenite-associated disseminated gold deposits in the Abitibi greenstone belt, Canada: Mineralium Deposita, v. 36, p. 503–516.

Roberts, R.G., and Morris, J.H., 1982, The geological setting of the Upper Beaver mine, Kirkland Lake district, Ontario: A copper-gold deposit in mafic volcanic rocks: Canadian Institute of Mining and Metallurgy, Special Volume 24, p. 73–82.

Roddick, J.C., 1987, Generalized numerical error analysis with applications to geochronology and thermodynamics: Geochimica Cosmochimica et Acta, v. 51, p. 2129–2135.

Stacey, J.S., and Kramers, J.D., 1975, Approximation of terrestrial lead isotope evolution by a two-stage model: Earth and Planetary Science Letters, v. 26, p. 207–221.

Steiger, R.H., and Jäger, E., 1977, Subcommission on geochronology: Convention on the use of decay constants in geo-and cosmochronology: Earth and Planetary Science Letters, v. 36, p. 359–362.

Sutton, J., Kontak, D., Côté-Mantha, O., and Beaudoin, G., 2023. Geology and mineral paragenesis of the Archean Upper Beaver oxidized intrusion-related Au-Cu deposit, Kirkland Lake Ontario: GAC-MAC-SGA 2023 Sudbury meeting Abstract Volume 46, Geoscience Canada, v. 50, p. 223.

Thomson, J.E., 1950. Geology of the main ore zone at Kirkland Lake: Ontario Department of Mines, Annual Report, v. 57, pt. 5, chapter 1, p. 55-103.

Van Kessel, A., 2018, Trace element geochemistry and Nd-Sr isotope systematics of scheelite from the Thunder Creek and 144 Gap deposits, Timmins, Ontario: implications for timing and genesis of gold: Unpublished MSc thesis, University of Western Ontario, London, Canada, 192 p.

Winchester, J.A., and Floyd, P.A., 1977, Geochemical discrimination of different magma series and their differentiation products using immobile elements: Chemical Geology, v. 20, p. 325-343.

York, D., 1969, Least-squares fitting of a straight line with correlated errors: Earth and Planetary Science Letters, v. 5, p. 320–324.

Zhang, J., Linnen, R., Lin, S., and Martin, R., 2011, New U-Pb zircon and monazite ages from the Matachewan Young-Davidson syenite-hosted gold deposits: A Mesoproterozoic thermal reactivation on the Neoarchean gold mineralization?: GAC-MAC-SEG-SGA Joint Annual Meeting, Abstracts Volume 34, p. 238.

Zhang, J., Lin, S., Linnen, R., and Martin, R., 2014, Structural setting of the Young-Davidson syenite-hosted gold deposit in the western Cadillac-Larder Lake deformation zone, Abitibi greenstone belt, Superior Province, Ontario: Precambrian Research, v. 248, p. 39–59.

Table 1. Chemical composition of the rocks dated in this study.

Analyte Symbol	Unit Symbol	Detection Limit	BF-BD-2016-001	PLBD-2018-019	PLBD-2018-039	PLBD-2018-052	PLBD-2018-056	BDPL-KL-2018-202	BDPL-KL-2018-201	UB-07-157	CH-919-14-DAT-01
SiO2	%	0.01	57.05	69.42	47.91	68.93	60.22	57.81	65.75	57.42	69.35
Al2O3	%	0.01	15.96	14.84	13.14	15.9	16.5	13.53	14.41	13.86	16.37
Fe2O3	%	0.01	3.11	0.91	6.83	0.55	0.86	2.07	0.8		< 0.01
FeO	%	0.1	1.5	0.5	1.8	0.4	1.6	2.8	2		1.1
MnO	%	0.001	0.056	0.02	0.181	0.029	0.072	0.095	0.077	0.08	0.091
MgO	%	0.01	3.58	0.38	3.75	0.24	1.2	2.79	1.72	3.35	0.96
CaO	%	0.01	2.72	2.37	7.44	0.74	3.29	4.68	2.75	5.06	2.5
Na2O	%	0.01	8.05	5.16	7.11	5.4	4.72	3.85	5.5	3.27	7.25
K2O	%	0.01	0.17	3.85	0.3	4.91	6.58	3.53	2.59	3.32	0.98
TiO2	%	0.001	0.554	0.175	0.718	0.086	0.175	0.464	0.4	0.44	0.155
P2O5	%	0.01	0.28	0.03	0.3	0.02	0.13	0.3	0.17	0.26	0.11
C-Total	%	0.01	0.87	0.22	2.77	0.25	1.24	1.74	0.39		
Total S	%	0.01	2.48	0.25	4.92	0.22	0.1	0.08	0.13		< 0.01
CO2	%	0.01	3.16	0.77	9.91	0.9	4.18	6.09	1.39	7.37	0.01
SO4	%	0.05	2.35	0.67	7.67	0.75	0.24	1.13	0.42		
LOI	%		5.95	2.23	9.3	1.42	4.63	7.21	2.83	8.13	0.27
LOI2	%		6.12	2.17	9.1	1.38	4.45	7.53	3.14		0.14
Total	%	0.01	99.15	99.93	98.97	98.67	100.2	99.43	100.1	99.84	99.1
Total 2	%	0.01	99.15	99.87	98.77	98.62	99.97	99.43	100.1		98.98
Fe2O3(T)	%	0.01	4.77	1.46	8.83	0.99	2.64	5.18	3.91	4.64	1.07
Zr	ppm	1	181	98	135	54	84	143	140	106	42
Y	ppm	0.5	10.8	2.1	22.2	3.4	13.1	15.6	19.4	12	5
Nb	ppm	0.2	4.6	1.5	6.7	2	5	4.1	6.2	5	0.4
Hf	ppm	0.1	3.9	3	3.2	1.6	2.2	3.7	3.9	3.20	1.3
Ta	ppm	0.01	0.24	0.07	0.33	0.18	0.24	0.37	0.42	0.30	2.07
Th	ppm	0.05	1.92	3.33	2.5	3.33	3.7	7.53	5.48	5.3	0.5
U	ppm	0.01	0.53	2.68	0.77	1.65	1.78	2.61	2.87	2	0.48
Ba	ppm	2	158	2027	24	1920	2524	1511	2048	2206	120
Rb	ppm	1	3	77	7	54	95	137	74	119	15
Sr	ppm	2	247	969	111	1058	1757	865	2978	895	339
Sc	ppm	1	5	2	21	< 1	4	11	8	11	4
Li	ppm	1	10	39	< 1	< 1	< 1	19	14		27
Be	ppm	1	< 1	2	1	2	2	2	3		10
B	ppm	1	5	24	15	14	15	22	4		41
V	ppm	5	25	13	52	6	37	91	47	94	33

Table 1. Chemical composition of the rocks dated in this study.

Analyte Symbol	Unit Symbol	Detection Limit	BF-BD-2016-001	PLBD-2018-019	PLBD-2018-039	PLBD-2018-052	PLBD-2018-056	BDPL-KL-2018-202	BDPL-KL-2018-201	UB-07-157	CH-919-14-DAT-01
Cr	ppm	1	47	7	69	32	58	82	66		14
Co	ppm	0.5	19.6	2.1	36.1	1	5.6	15.4	9.8		1.2
Ni	ppm	1	60	3	108	3	29	38	31		8
Cu	ppm	0.5	52.4	26.1	7.1	10.1	5.1	58.1	21.9		0.7
Zn	ppm	0.5	17.1	30.1	55	11.3	48.4	85	84.5		26.9
Pb	ppm	2	7	14	6	15	30	14	18		8
Cd	ppm	0.2	< 0.2	< 0.2	< 0.2	< 0.2	< 0.2	< 0.2	< 0.2		0.3
Ga	ppm	1	15	20	24	22	21	18	19	22	18
Ge	ppm	0.5	< 0.5	0.7	1	1.2	1.3	1.1	1		1
Au	ppb	5	> 5000	100	> 5000	134	27	5	< 5	11	25
Au	g/t	0.03	6.32		6.08						
Ag	ppm	0.5	0.8	< 0.5	2.4	< 0.5	< 0.5	0.6	0.8		< 0.5
As	ppm	0.1	60.6	< 0.1	1.2	0.2	< 0.1	3.1	9.3	2.50	77.6
Sb	ppm	0.02	0.33	< 0.02	< 0.02	< 0.02	< 0.02	1.23	0.31		0.07
Hg	ppb	5	44	< 5	10	9	< 5	< 5	< 5		
Bi	ppm	0.02	0.38	0.32	2.65	0.18	0.27	0.24	0.48		0.2
Tl	ppm	0.05	< 0.05	0.38	< 0.05	0.6	0.67	0.73	0.45		< 0.05
Se	ppm	0.1	1.2	0.1	1.5	< 0.1	< 0.1	< 0.1	< 0.1		0.1
Te	ppm	0.02	0.21	0.04	6.49	0.18	0.08	0.09	< 0.02		< 0.02
Sn	ppm	1	< 1	< 1	1	< 1	< 1	< 1	1		4
W	ppm	0.5	9.9	7	45.3	6.8	11.5	0.8	< 0.5		14.5
Mo	ppm	1	9	< 1	121	51	3	< 1	< 1		< 1
Cs	ppm	0.1	0.1	1.8	0.2	0.4	0.3	3.8	1.8		1
In	ppm	0.1	< 0.1	< 0.1	< 0.1	< 0.1	< 0.1	< 0.1	< 0.1		< 0.1
Mn	ppm	2	395	130	1400	149	488	720	544		666
La	ppm	0.05	21.7	17.9	12.1	3.93	28.8	43.7	30.2	28.90	1.76
Ce	ppm	0.05	45.3	39.7	26.4	10.9	76.3	83.5	60	62.00	5.34
Pr	ppm	0.01	5.06	4.75	3.55	1.53	9.31	9.64	7.1	6.59	0.82
Nd	ppm	0.05	21.2	18.4	16.7	6.8	37.5	38.8	29.7	25.00	3.46
Sm	ppm	0.01	3.59	2.86	4.56	1.47	6.61	6.59	5.52	5.30	1.13
Eu	ppm	0.005	0.918	0.632	1.6	0.421	1.75	1.66	1.47	1.40	0.233
Gd	ppm	0.01	2.92	1.23	4.87	1.04	4.44	4.54	4.46	3.80	0.91
Tb	ppm	0.01	0.36	0.12	0.7	0.14	0.5	0.57	0.63	0.50	0.16
Dy	ppm	0.01	1.84	0.44	3.84	0.58	2.46	2.88	3.43	2.20	0.97
Ho	ppm	0.01	0.37	0.06	0.74	0.1	0.41	0.52	0.68	0.40	0.19
Er	ppm	0.01	1.1	0.18	2.05	0.26	1.1	1.5	1.87	1.10	0.56
Tm	ppm	0.005	0.17	0.026	0.321	0.037	0.152	0.205	0.271	0.15	0.095

Table 1. Chemical composition of the rocks dated in this study.

Analyte Symbol	Unit Symbol	Detection Limit	BF-BD-2016-001	PLBD-2018-019	PLBD-2018-039	PLBD-2018-052	PLBD-2018-056	BDPL-KL-2018-202	BDPL-KL-2018-201	UB-07-157	CH-919-14-DAT-01
Yb	ppm	0.01	1.05	0.17	2.11	0.24	0.99	1.33	1.82	0.90	0.65
Lu	ppm	0.002	0.161	0.024	0.341	0.035	0.159	0.212	0.286	0.15	0.095

Analytical methods

Whole-rock analyses were performed at Activation Laboratories Ltd. in Ancaster, Ontario, using a combination of their standard preparation and analytical packages, the details of which can be found at https://actlabs.com/geochemistry/lithogeochemistry-and-whole-rock-analyis.

Samples were initially dried (60°C) and crushed to at least 90% (<2mm) in a steel jaw crusher. A mechanically split fraction was pulverized in a chromium-free steel mill until 95% of the sample material passed through a 74 µm mesh. Major elements were determined by lithium metaborate-tetraborate fusion followed by inductively coupled plasma mass spectrometry (ICP-MS; FUS-MS). Trace and rare earth elements were determined by a combination of lithium metaborate-tetraborate and total digestion (four acids) followed by inductively coupled plasma mass spectrometry (ICP-MS; FUS-MS) and inductively coupled plasma atomic emission spectrometry (ICP-OES; FUS-ICP). FeO was determined by titration using a cold acid digestion (ammonium metavanadate and hydrofluoric acid) in an open system (TITR).

For chalcophile elements a four-acid digestion ICP-MS (TD-MS) method was preferred. Aqua regia (AR-MS) digestion coupled with ICP-MS was chosen to analyze As, Sb, Bi, Se and Te. Boron was determined by gamma neutron activation analysis (PGNAA). Gold and silver were measured by a combination of atomic absorption (FA-AA), fire assay, and gravimetry (FA-GRAV). High-grade ore zone samples were re-analyzed with a combination of fire assay and gravimetric methods for gold and silver (FA-GRAV) and aqua regia dissolution (ICP-OES) or sodium peroxide fusion (FUS-Na2O2) with ICP-OES depending on the analyte. CO2 and Total (S) were determined by combustion infrared analysis (IR). Fluorine was determined by lithium metaborate and tetraborate fusion and fluoride ion electrode analysis (FUS-ISE). Chlorine was determined by instrumental neutron activation analysis (INAA). Mercury was determined by cold vapour flow injection (FIMS) following aqua regia digestion.

Actlabs reports LOI, LOI2, Total and Total 2. LOI is determined by weighing a small amount of the sample before and after ignition. However, because FeO was measured, it was possible to adjust LOI to take into account the weight gain resulting from oxidation of FeO to Fe2O3. This adjusted value of LOI is LOI2. Total1 is the total of all major oxides using Fe2O3(T) and LOI, whereas Total2 includes LOI2.

Table 2. Zircon CA-ID-TIMS U-Pb isotopic data for selected Abitibi intrusive units, Québec and Ontario. Data from the Jack Satterly Geochronology Laboratory, University of Toronto.

Fraction	Description	U (ppm)	Pb^T (pg)	Pb_C (pg)	Th/U	$^{206}Pb/^{204}Pb$	$^{206}Pb/^{238}U$	± 2s	$^{207}Pb/^{235}U$	± 2s	$^{207}Pb/^{206}Pb$	± 2s	Ages (Ma) $^{206}Pb/^{238}U$	± 2s	$^{207}Pb/^{235}U$	± 2s	$^{207}Pb/^{206}Pb$	± 2s	Disc. (%)
BFBD-2016-001; Pre-ore, intermediate dyke, Black Fox mine, Matheson area																			
Z1	1 lrg pink-pbr, short sharp pr	75	44.99	0.39	0.556	6361	0.520751	0.001276	13.31572	0.03710	0.185453	0.000192	2702.4	5.4	2702.3	2.6	2702.2	1.7	0.0
Z2	1 lrg clr cls gemmy pr	74	46.35	1.06	0.772	2349	0.520301	0.001230	13.30686	0.04055	0.185490	0.000273	2700.5	5.2	2701.7	2.9	2702.6	2.4	0.1
Z3	1 clr, cls subeq pr	46	28.26	0.37	0.670	4202	0.521290	0.001619	13.33166	0.04519	0.185483	0.000237	2704.6	6.9	2703.4	3.2	2702.5	2.1	-0.1
Z4	1 clr, cls spindle, fctd/gemmy	71	44.98	1.19	0.802	2019	0.520238	0.001469	13.30116	0.04733	0.185433	0.000291	2700.2	6.2	2701.3	3.4	2702.1	2.6	0.1
Z5	1 clr, cls, sm, spindle	56	35.42	0.32	0.842	5860	0.520090	0.001492	13.29949	0.04223	0.185462	0.000198	2699.6	6.3	2701.1	3.0	2702.3	1.8	0.1
PLDB-2018-019; Pink feldspar porphyry, O'Brien intrusion, Bachelor mine																			
Z1	1 large, blocky	132	140.34	5.79	0.073	1519	0.514783	0.001076	13.06039	0.03336	0.184005	0.000371	2677.0	4.6	2684.0	3.1	2689.3	3.3	0.6
Z2	1 2:1 cldy doubly-term pr	173	91.68	0.27	0.069	21455	0.512882	0.001172	12.99459	0.03223	0.183757	0.000227	2668.9	5.0	2679.3	2.3	2687.1	2.0	0.8
Z3	1 glassy rect block	161	86.40	0.25	0.082	21600	0.516463	0.001084	13.11321	0.03203	0.184149	0.000166	2684.2	4.6	2687.8	2.3	2690.6	1.5	0.3
Z4	1 lrg glassy block	166	88.99	0.29	0.080	18871	0.517702	0.000969	13.12843	0.03059	0.183921	0.000158	2689.4	4.1	2688.9	2.2	2688.5	1.4	0.0
Z5	1 sm glassy block	99	53.16	0.26	0.080	12555	0.517349	0.001087	13.13935	0.03359	0.184200	0.000177	2687.9	4.6	2689.7	2.4	2691.1	1.6	0.1
Z6	1 brkn, cls, sl cldy, rect frag	56	29.90	0.78	0.105	2377	0.514045	0.001451	13.03541	0.04546	0.183917	0.000281	2673.9	6.2	2682.2	3.3	2688.5	2.5	0.7
PLDB-2018-056; Porphyritic syenite, West Timmins complex, HWY-144 deposit (144 GAP)																			
Z2	1 vsm, blocky frag	46	14.91	1.08	0.985	723	0.515168	0.002597	12.98545	0.09121	0.182813	0.000728	2678.7	11.0	2678.6	6.6	2678.6	6.6	0.0
Z3	1 vsm, blocky frag	21	11.79	1.14	0.339	623	0.521178	0.002889	13.19967	0.10486	0.183686	0.000831	2704.2	12.2	2694.0	7.5	2686.4	7.5	-0.8
Z4	1 small, cldy, blocky frag	57	32.74	0.35	0.421	5376	0.512280	0.001358	12.92230	0.03890	0.182950	0.000188	2666.4	5.8	2674.0	2.8	2679.8	1.7	0.6
Z5	1 wispy clr cls shard	15	3.10	0.50	0.328	379	0.515429	0.009847	12.98225	0.27623	0.182675	0.001374	2679.8	41.8	2678.4	20.0	2677.3	12.5	-0.1
BDPL-KL-2018-202; Moderately to strongly altered, porphyritic syenite, ore zone host, Macassa mine, Kirkland Lake																			
Z1	1 clr, wide, stubby pr	52	33.86	2.43	0.936	738	0.520528	0.001504	13.28107	0.07430	0.185049	0.000697	2701.4	6.4	2699.8	5.3	2698.7	6.2	-0.1
Z2	1 clr cls pr	33	19.40	2.49	0.518	456	0.520497	0.002297	13.28399	0.11761	0.185101	0.001160	2701.3	9.7	2700.0	8.4	2699.1	10.4	-0.1
Z3	1 el, clr, cls 'tip'	50	14.82	0.26	0.515	3171	0.517123	0.002356	13.09801	0.06368	0.183701	0.000225	2687.0	10.0	2686.7	4.6	2686.6	2.0	0.0
Z4	2 thin, vsm, el, cls, clr pr frags	58	6.86	1.84	0.465	230	0.525205	0.005170	13.29901	0.24582	0.183649	0.002311	2721.2	21.8	2701.1	17.5	2686.1	20.9	-1.6
Z5	1 clr, glassy tip	48	11.27	0.27	0.462	2425	0.518590	0.003023	13.18058	0.08048	0.184335	0.000291	2693.2	12.8	2692.7	5.8	2692.3	2.6	0.0
Z6	1 sm, straight, clr, cls brkn pr	44	12.56	0.23	0.335	3224	0.517726	0.002668	13.11365	0.07096	0.183705	0.000238	2689.5	11.3	2687.9	5.1	2686.6	2.1	-0.1
Z7	1 mixed grey cldy & clr, cls pr	55	12.79	0.61	0.449	1216	0.519501	0.002687	13.20251	0.07954	0.184319	0.000451	2697.1	11.4	2694.2	5.7	2692.1	4.0	-0.2
BDPL-KL-2018-201; Less altered feldspar-phyric syenite, Macassa 04 Break mine, Kirkland Lake																			
Z1	1 sm, clr, cls, 2:1, fl, axial incl	50	14.62	0.47	0.462	1788	0.516740	0.002409	13.06809	0.06789	0.183417	0.000329	2685.3	10.2	2684.6	4.9	2684.0	3.0	-0.1
Z2	1 sm, needle, cldy etched	56	11.77	0.14	0.634	4734	0.516571	0.002927	13.02255	0.07608	0.182837	0.000203	2684.6	12.4	2681.3	5.5	2678.8	1.8	-0.3
Z3	1 sm eq, fctd, cldy pr	22	14.10	0.27	0.778	2753	0.521881	0.002657	13.28391	0.07166	0.184609	0.000287	2707.2	11.3	2700.0	5.1	2694.7	2.6	-0.6
Z4	1 'lrg', cldy 2:1 pr	201	118.57	0.30	0.533	21851	0.515570	0.000980	13.00996	0.03018	0.183015	0.000142	2680.4	4.2	2680.4	2.2	2680.4	1.3	0.0
Z5	1 sm, cldy, brkn el pr	114	67.08	0.32	0.527	11892	0.514670	0.001092	12.95662	0.03179	0.182584	0.000182	2676.5	4.6	2676.5	2.3	2676.5	1.6	0.0
Z6	1 sm, cldy, brkn el pr	227	45.51	0.43	1.174	5220	0.514608	0.001285	12.95925	0.03711	0.182643	0.000195	2676.3	5.5	2676.7	2.7	2677.0	1.8	0.0
Z7	1 sm, cldy, brkn el pr	57	35.66	1.04	0.791	1839	0.514742	0.001454	12.95558	0.04686	0.182543	0.000320	2676.8	6.2	2676.4	3.4	2676.1	2.9	0.0

Notes:

All analyzed fractions represent best optical quality (crack-, inclusion-, core-free), fresh (least altered) grains of zircon. Zircons were chemically abraded using modified protocols after Mattinson (2005).

Abbreviations: Z - zircon; clr - clear; cls - colourless; cldy - cloudy; fctd - faceted, fl - flat; frags - fragments; pr - prism/prismatic; el - elongate; eq - equant; sm - small; vsm- very small; lrg - large; incl - inclusion; brkn - bro

Pb^T is total amount (in picograms) of Pb.

Pb_C is total measured common Pb (in picograms) assuming the isotopic composition of laboratory blank: 206/204 - 18.49±0.4%; 207/204 - 15.59±0.4%; 208/204 - 39.36±0.4%.

Pb/U atomic ratios are corrected for spike, fractionation, blank, and, where necessary, initial common Pb; 206Pb/204Pb is corrected for spike and fractionation.

Th/U is model value calculated from radiogenic 208Pb/206Pb ratio and 207Pb/206Pb age, assuming concordance.

Disc. (%) - per cent discordance for the given 207Pb/206Pb age.

Uranium decay constants are from Jaffey et al. (1971).

Table 3. U-Pb zircon ID-TIMS analytical data, Geological Survey of Canada, Ottawa.

Fraction[1]	Description[2]	U[3] (ppm)	Pb[4] (ppm)	$^{206}Pb/^{204}Pb$[5]	Pb[6] pg	Isotopic Ratios[7] $^{208}Pb/^{206}Pb$	$^{207}Pb/^{235}U$	±1σ (abs)	$^{206}Pb/^{238}U$	±1σ (abs)	Corr.[8] Coeff.	$^{207}Pb/^{206}Pb$	±1σ (abs)	Dates (Ma)[9] $^{206}Pb/^{238}U$	±2σ (abs)	$^{207}Pb/^{235}U$	±2σ (abs)	$^{207}Pb/^{206}Pb$	±2σ (abs)	% Disc
UB-07-157 (z9449) Diorite (*spotted porphyry*) (drill core UB-07-98, 570 m depth), Upper Beaver deposit, Larder Lake																				
A1 (1)	pBr,Clr,Eu,Pr,Osc,rFr,PA1.5	264	157	4538	2.23	0.17	12.852	0.015	0.51004	0.00049	0.931	0.18276	0.00008	2656.8	4.2	2668.9	2.2	2678.1	1.5	1.0
A2 (1)	pBr,Clr,Eu,Pr,Osc,rFr,rIn,PA1.5	176	104	453	10.30	0.16	12.964	0.040	0.51211	0.00169	0.877	0.18360	0.00029	2665.6	14.4	2677.1	5.8	2685.7	5.3	0.9
A3 (1)	pBr,Clr,Eu,Pr,Osc,fFr,PA1.5	258	151	6271	1.83	0.15	12.830	0.015	0.50928	0.00048	0.943	0.18271	0.00008	2653.5	4.1	2667.2	2.2	2677.6	1.4	1.1
A4 (1)	pBr,Clr,Eu,Pr,Osc,rFr,PA1.5	278	167	3419	1.81	0.19	12.841	0.015	0.50938	0.00050	0.920	0.18283	0.00009	2654.0	4.2	2668.0	2.3	2678.7	1.6	1.1
A5 (1)	pBr,Clr,Eu,Pr,rFr,PA1.5	124	74	492	6.69	0.16	13.017	0.028	0.51604	0.00092	0.825	0.18294	0.00022	2682.4	7.8	2680.9	4.0	2679.7	4.0	-0.1
A6 (1)	pBr,Clr,Eu,Pr,fFr,rIn,PA1.5	262	151	1419	4.04	0.17	12.472	0.017	0.49578	0.00054	0.889	0.18245	0.00011	2595.6	4.7	2640.6	2.5	2675.3	2.1	3.6
Z1A (1)	pBr,Clr,Eu,Pr,Osc,fFr,CA3	228	126	2129	7.77	0.15	12.166	0.015	0.48388	0.00044	0.914	0.18236	0.00010	2544.1	3.8	2617.3	2.3	2674.4	1.7	5.9
Z1B (1)	Br,Clr,Eu,Pr,Osc,fFr,rIn,CA3	317	185	2212	7.41	0.14	12.950	0.016	0.51501	0.00054	0.917	0.18237	0.00009	2678.0	4.6	2676.0	2.4	2674.5	1.7	-0.2
Z1C (1)	pBr,Clr,Eu,St,rFr,rIn,CA6	175	102	6734	3.31	0.15	12.789	0.015	0.50742	0.00047	0.942	0.18280	0.00008	2645.6	4.0	2664.3	2.2	2678.5	1.4	1.5
Z1D (1)	pBr,Clr,Su,Tip,Osc,fFr,CA8	390	228	5916	2.11	0.14	12.936	0.015	0.51318	0.00049	0.944	0.18282	0.00008	2670.2	4.1	2675.0	2.2	2678.6	1.4	0.4
Z2A (1)	pBr,Clr,Eu,St,Osc,rFr,rIn,CA3	200	117	3015	3.31	0.18	12.615	0.017	0.49996	0.00059	0.882	0.18301	0.00012	2613.6	5.1	2651.4	2.5	2680.3	2.1	3.0
Z2B (1)	pBr,Clr,Su,St,fFr,rIn,CA6	170	101	10508	0.50	0.16	12.912	0.015	0.51252	0.00046	0.939	0.18272	0.00008	2667.4	3.9	2673.3	2.2	2677.7	1.4	0.5
Z2C (1)	pBr,Clr,Eu,St,fFr,CA8	175	102	3437	2.77	0.14	12.910	0.016	0.51234	0.00051	0.937	0.18276	0.00008	2666.6	4.3	2673.1	2.3	2678.1	1.5	0.5
CH919-14-DAT-01 (z11241) Cheechoo intrusion																				
A6-1 (1)	Br,Tu,Su,St,fFr,rIn,CA6	51	22	7519	1.14	0.02	9.576	0.011	0.42331	0.00040	0.938	0.16407	0.00007	2275.5	3.6	2394.9	2.2	2498.0	1.5	10.6
A16-1 (1)	Br,Clr,Eu,Seq,fFr,CA16	181	93	13638	1.32	0.02	12.079	0.014	0.49879	0.00047	0.926	0.17564	0.00008	2608.6	4.0	2610.6	2.2	2612.1	1.5	0.2
A16-2 (1)	Co,Clr,Su,Pr,fFr,CA16	58	33	7777	1.00	0.08	13.376	0.016	0.52168	0.00053	0.894	0.18596	0.00010	2706.3	4.5	2706.6	2.3	2706.8	1.8	0.0
A16-3 (1)	Br,Clr,Eu,Pr,CA16	242	124	25335	1.15	0.02	12.072	0.014	0.49840	0.00044	0.946	0.17567	0.00007	2606.9	3.8	2610.0	2.1	2612.4	1.4	0.3
A16-4 (1)	Br,Clr,Su,Seq,fFr,rIn,CA16	123	63	10305	0.97	0.02	12.041	0.014	0.49712	0.00047	0.920	0.17566	0.00008	2601.4	4.0	2607.6	2.2	2612.3	1.6	0.5
B16-1 (1)	Br,Clr,An,Frag,rIn,CA16	87	44	8737	0.89	0.02	12.048	0.016	0.49811	0.00055	0.951	0.17542	0.00008	2605.7	4.8	2608.1	2.5	2610.0	1.4	0.2

Notes:

[1]Number in bracket refers to the number of zircon grains in the analysis.

[2]Fraction descriptions: pBr=pale brown; Br=brown; Co=colourless; Clr=clear; Tu=Turbid; Eu=euhedral; Su=subhedral; An=anhedral; Pr=prismatic; St=stubby prism; Seq=Subequant; Frag=fragment; Osc=oscillatory zoning;

rFr=rare fractures; fFr=few fractures; rIn=Rare Inclusions.

PA1.5=physically abraded for 1.5 hours; CA3=chemically abraded for 3 hours.

[3]U concentration subject to uncertainty up to ~50% in weight of grains.

[4]Radiogenic Pb.

[5]Measured ratio, corrected for spike and fractionation.

[6]Total common Pb in analysis corrected for fractionation and spike.

[7]Corrected for blank Pb and U and common Pb, errors quoted are 1 sigma absolute; procedural blank values ranged from 0.9-2.8 pg for Pb (with one exception at 13.1 pg); Pb blank isotopic composition ($^{206}Pb/^{204}Pb$ = 18.206 ± 0.47, $^{207}Pb/^{204}Pb$ = 15.376 ± 0.14, and $^{208}Pb/^{204}Pb$ = 37.406 ± 0.19) is based on the analysis of procedural blanks; corrections for common Pb were made using Cummings and Richards (1975) compositions.

[8]Correlation Coefficient

[9]Corrected for blank and common Pb, errors quoted are 2 sigma in Ma. Dates (Ma) calculated using $^{238}U/^{235}U$ = 137.88 as recommended by Steiger and Jäger (1977) and decay constants of $^{238}U = 1.55125 \times 10^{-10}$ year^{-1} and $^{235}U = 9.8485 \times 10^{-10}$ year^{-1} from Jaffey et al. (1971).

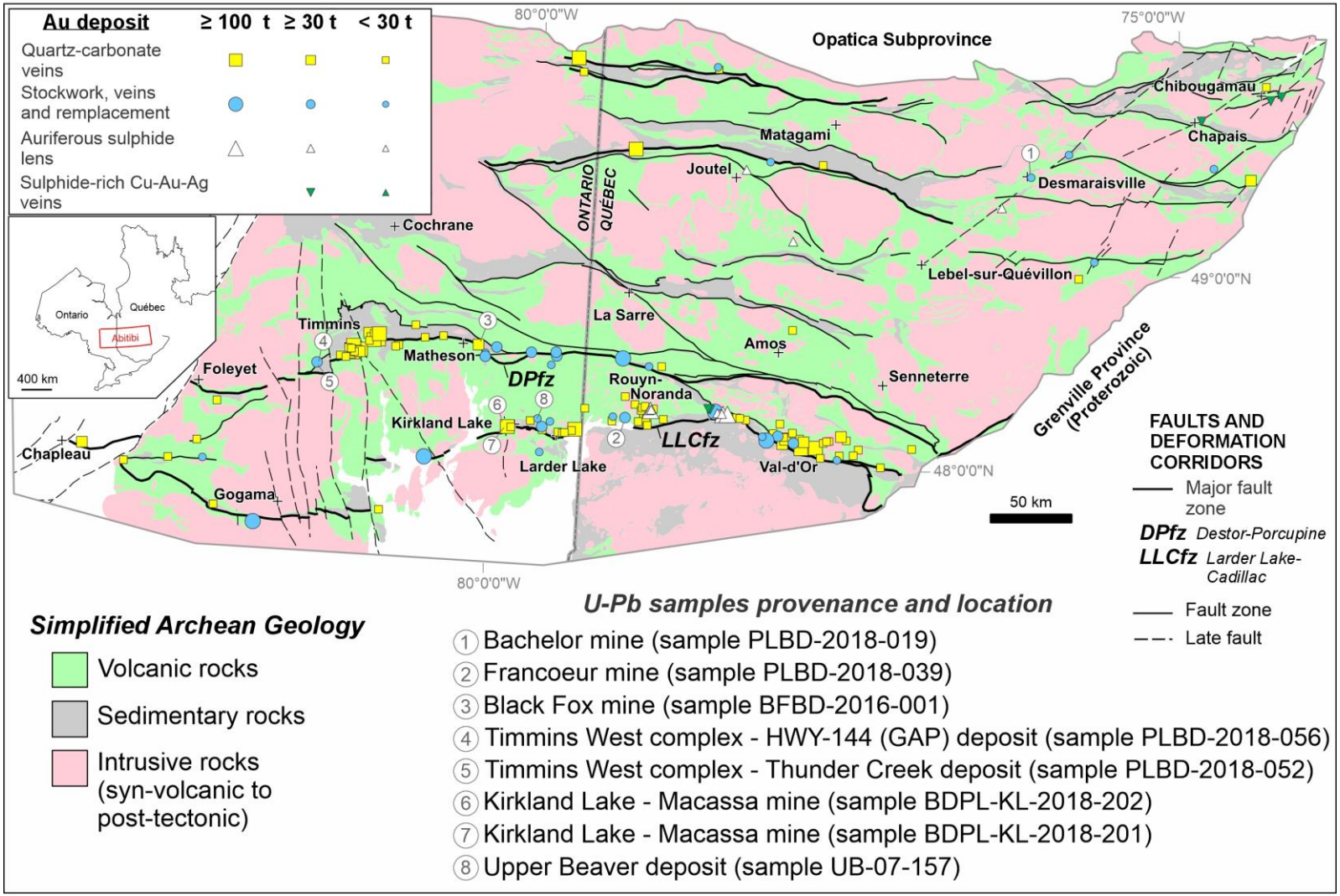

Figure 1. Simplified geologic map of the Abitibi greenstone belt showing the distribution of gold deposits with over 100,000 ounces of gold, and the location of the samples dated in this study. Modified from Dubé and Mercier-Langevin (2020), Mercier-Langevin et al. (2022, 2023). See Dubé and Mercier-Langevin (2020) for deposits classification and descriptions.

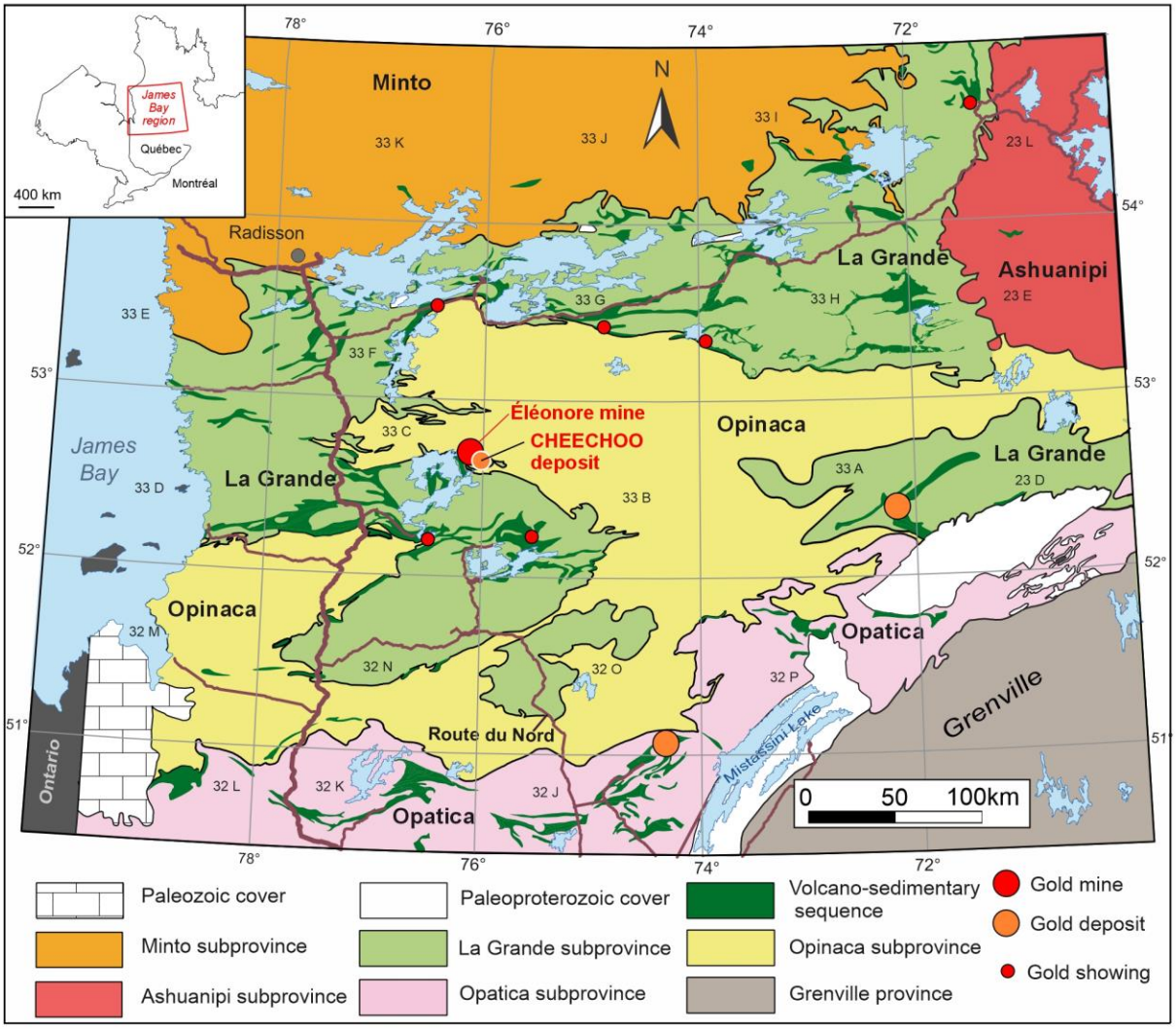

Figure 2. Simplified geologic map of the Eeyou Istchee James Bay area of nothern Quebec showing the location of the Éléonore mine and the Cheechoo gold deposit, approximately 15 km southeast of the Éléonore mine. Figure from Fontaine et al. (2015).

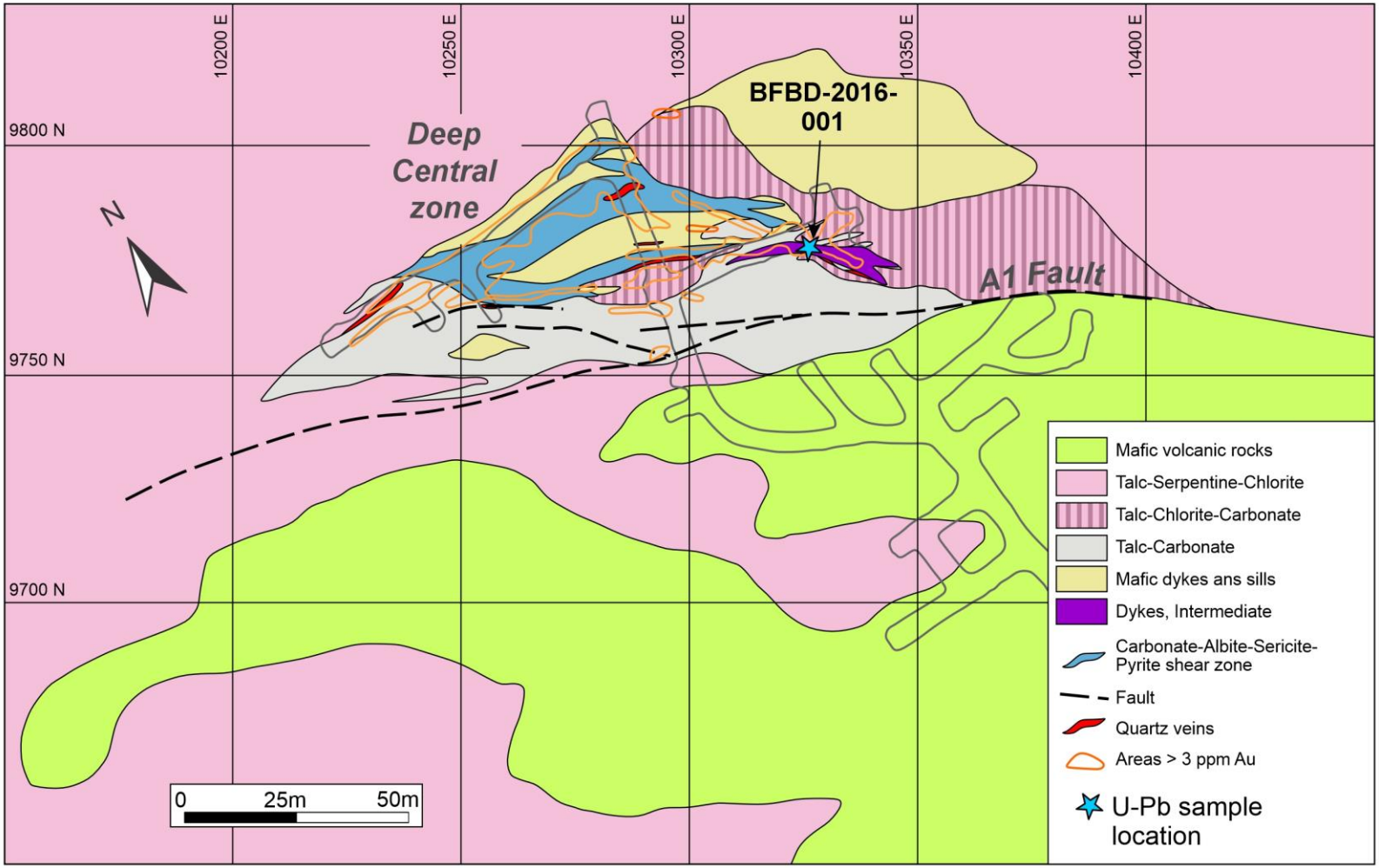

Figure 3. Geologic map of 680 level east of the Black Fox mine (spot 3 on Fig. 1), Deep Central zone. The location of sample BFBD-2016-001 is shown. Figure is courtesy of, and compiled from underground mapping and drilling interpretation by, D. Rhys (Panterra Geoservices Inc.), shown with permission of McEwen Mining.

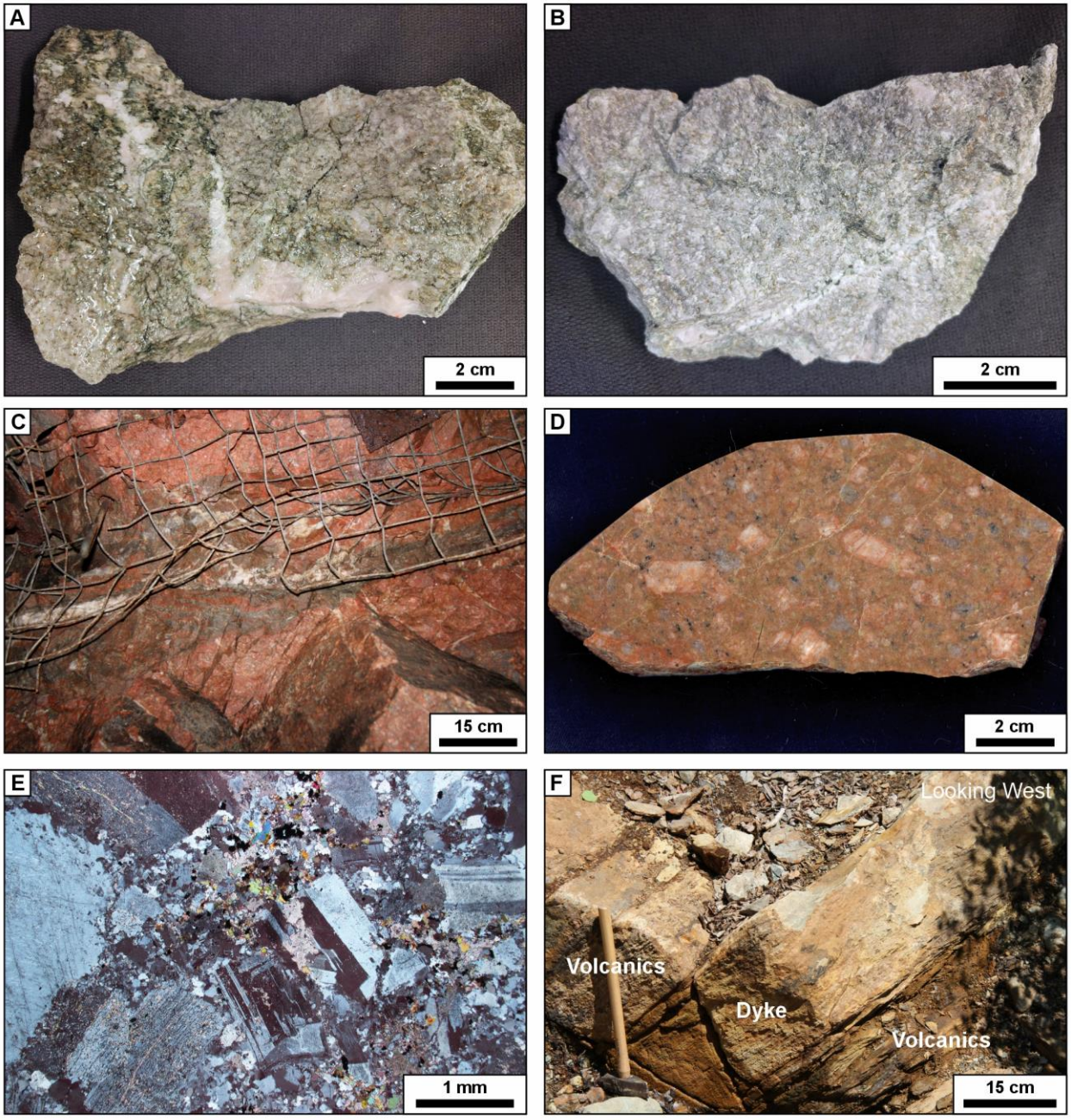

Figure 4. Photographs of dated samples and sampling sites. See text for details. **A.** Sample BFBD-2016-001, Black Fox mine, wet surface. Photograph by P. Mercier-Langevin, NRCan photo 2023-389. **B.** Sample BFBD-2016-001, dry surface. Photograph by P. Mercier-Langevin, NRCan photo 2023-390 **C.** Mineralized structure in the O'Brien intrusion, a few meters away from sample PLBD-2018-019 sampling site, Bachelor mine. Photograph by B. Dubé, NRCan photo 2023-391. **D.** Sample PLBD-2018-019. Photograph by B. Dubé, NRCan photo 2023-392. **E.** Sample PLBD-2018-019, photomicrograph, polarized light, Photograph by P. Mercier-Langevin, NRCan photo 2023-393. **F.** Sample PLBD-2018-039 sampling site, Francoeur mine. Photograph by B. Dubé, NRCan photo 2023-394.

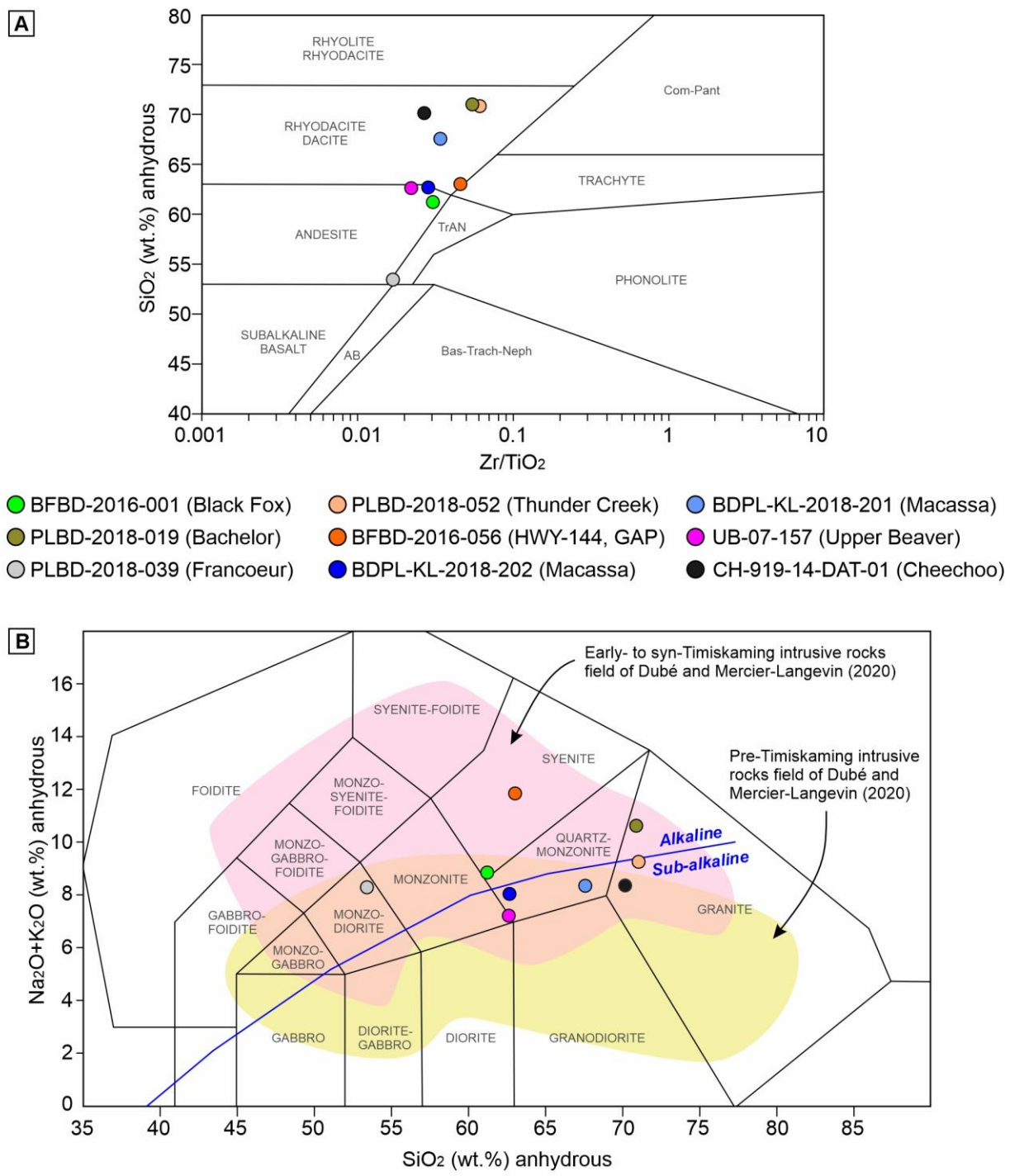

Figure 5. A. Winchester and Floyd (1977) classification diagram. Although calibrated for sub-alkaline volcanic rocks, this diagram allows to quickly assess rock composition. **B.** Total alkali silica classification diagram for magmatic rocks from Middemost (1994).

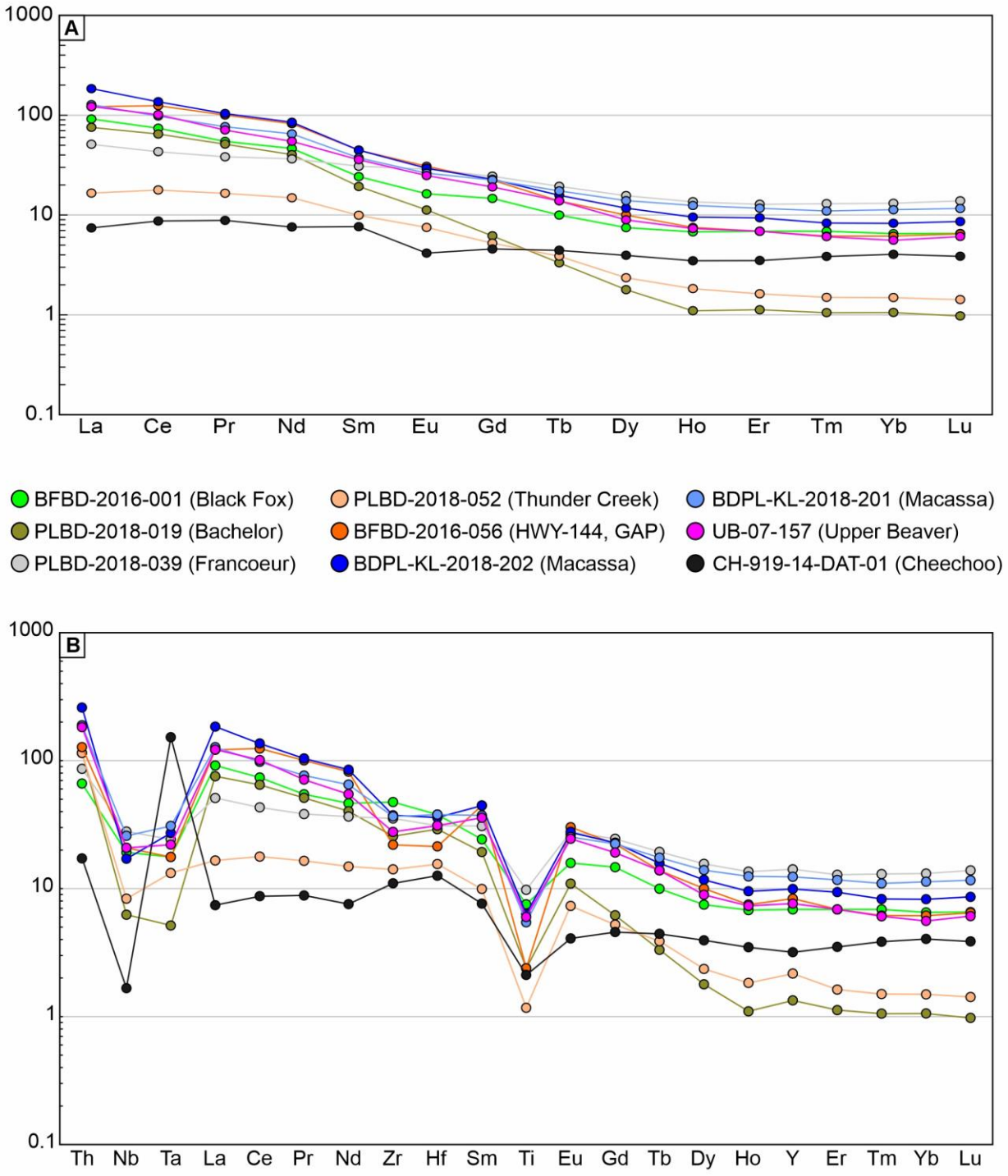

Figure 6. A. Rare-earth elements diagram, normalized on C1 chondrite values from McDonough and Sun (1995). **B.** Multi-element (high field strenght elements and rare-earth elements) diagram, modified from Pearce (2008). Values normalized on C1 chrondrite (McDonough and Sun, 1995).

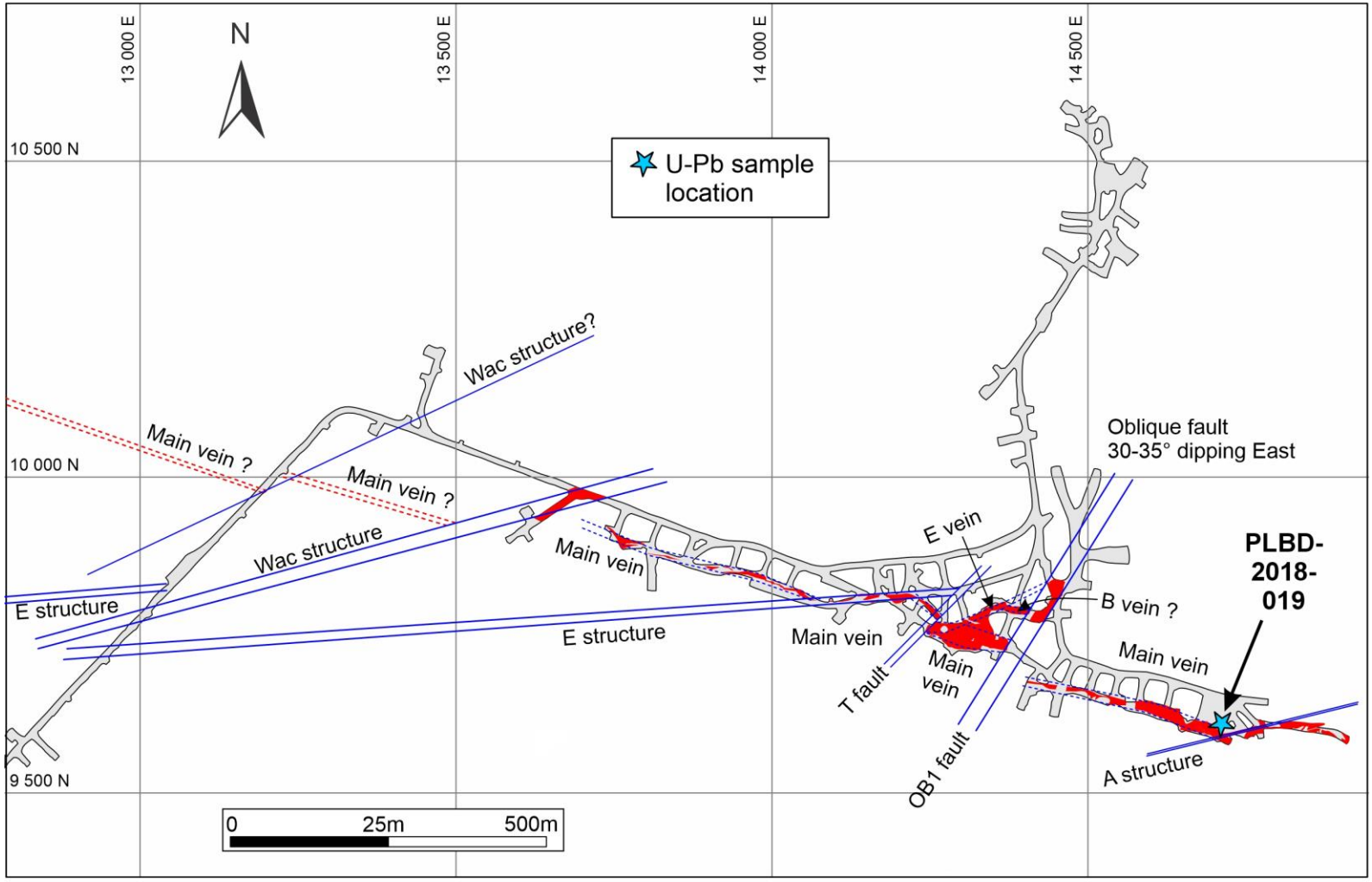

Figure 7. Geologic map of level 14 of the Bachelor mine (spot 1 in Fig. 1), Main zone. The location of sample PLBD-2018-019 is shown. Figure courtesy of Bonterra Resources inc.

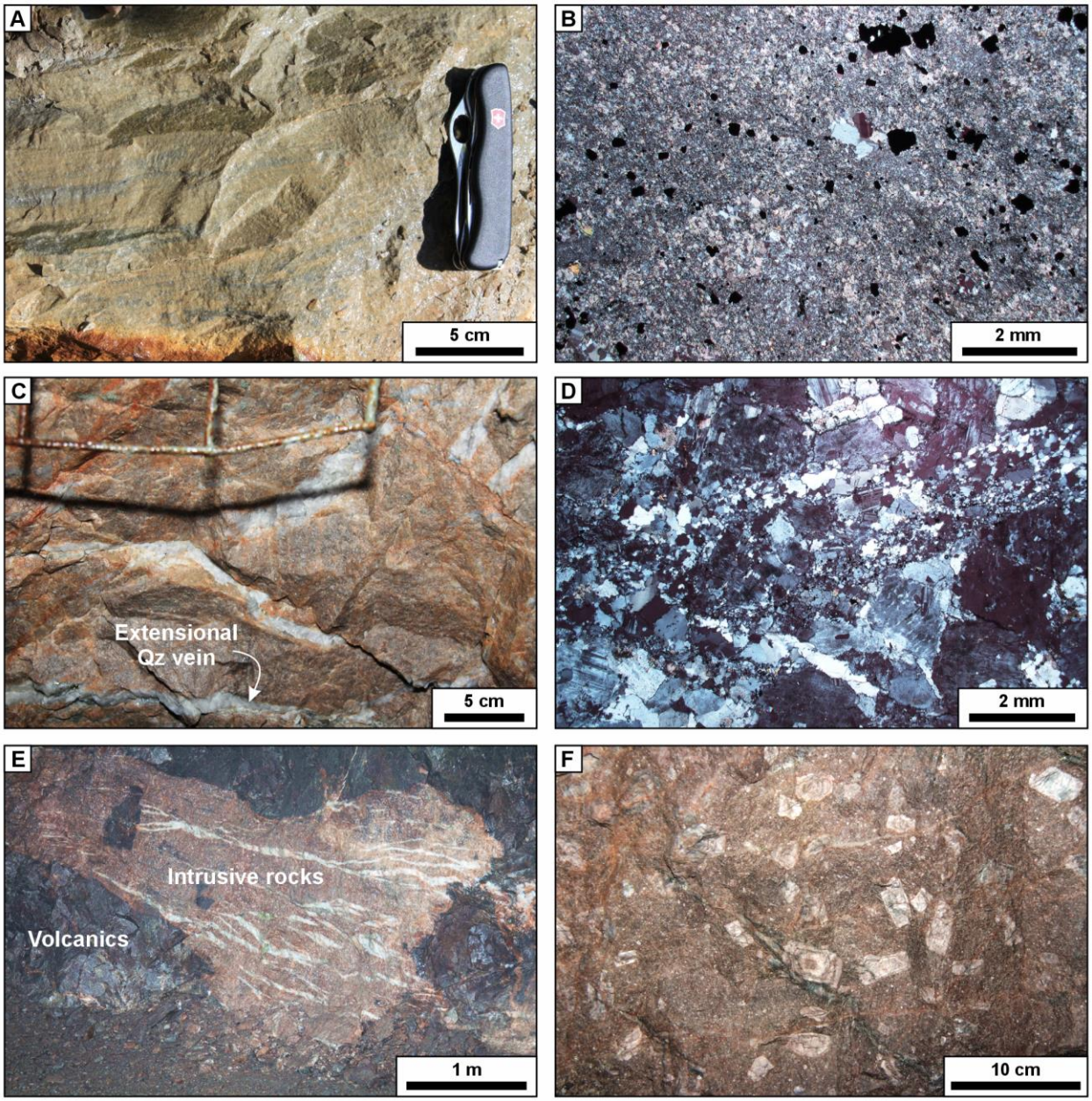

Figure 8. Photographs of dated samples and sampling sites. See text for details. **A.** Sample PLBD-2018-039, Francoeur mine. Photograph by P. Mercier-Langevin, NRCan photo 2023-395. **B.** Sample PLBD-2018-039, photomicrograph, polarized light. Photograph by P. Mercier-Langevin, NRCan photo 2023-396. **C.** Sample PLBD-2018-052 sampling site, Thunder Creek deposit. Photograph by P. Mercier-Langevin, NRCan photo 2023-397. **D.** Sample PLBD-2018-052, photomicrograph, polarized light. Photograph by P. Mercier-Langevin, NRCan photo 2023-398. **E.** Sample PLBD-2018-056 sampling area, HWY-144 (144 GAP) deposit. Photograph by P. Mercier-Langevin, NRCan photo 2023-399. **F.** Sample PLBD-2018-056 sampling site. Photograph by B. Dubé, NRCan photo 2023-400.

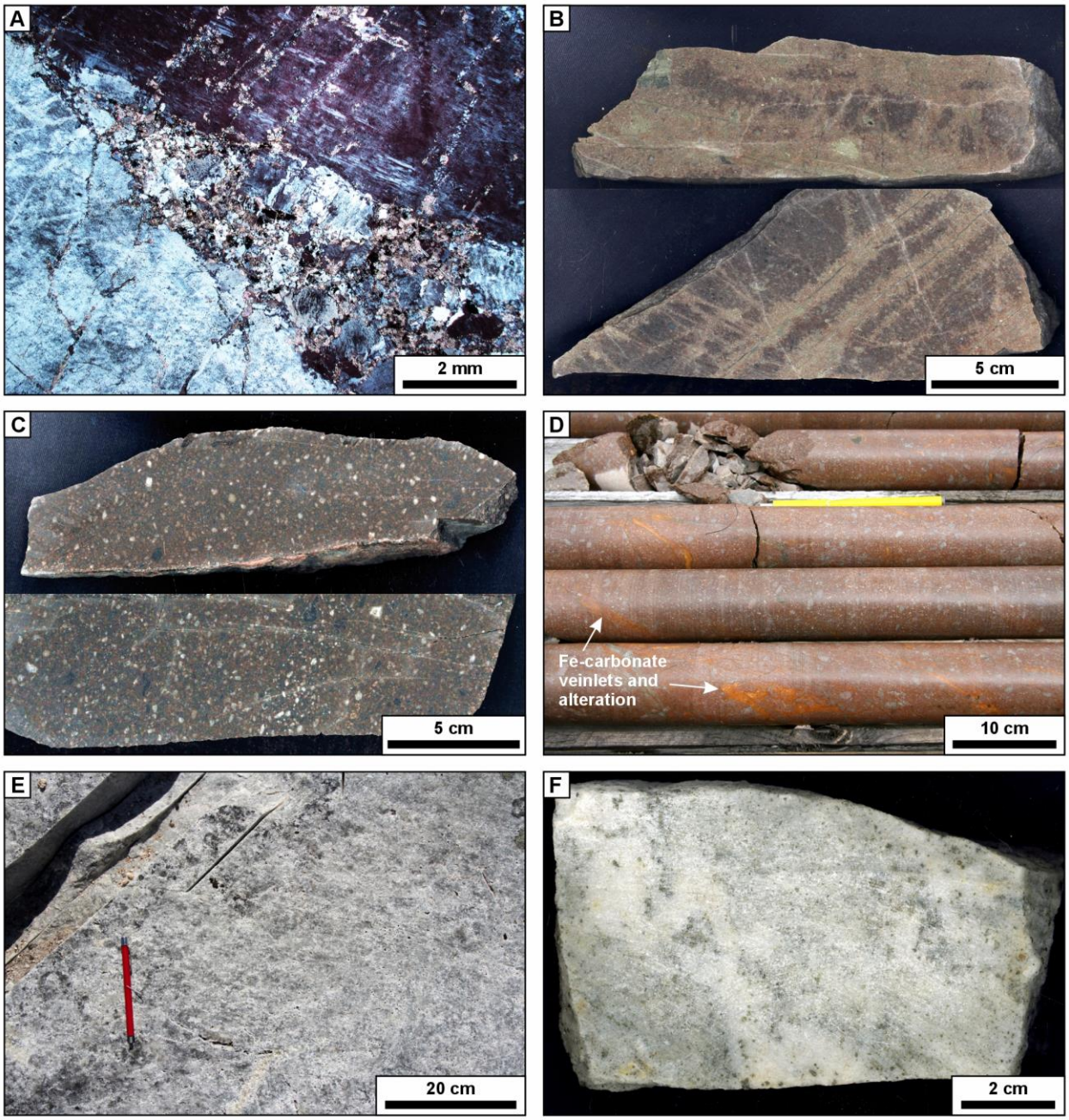

Figure 9. Photographs of dated samples and sampling sites. See text for details. **A.** Sample PLBD-2018-056, photomicrograph, polarized light. Photograph by P. Mercier-Langevin, NRCan photo 2023-401. **B.** Sample BDPL-KL-2018-202, Macassa deposit. Photograph by B. Dubé, NRCan photo 2023-402. **C.** Sample BDPL-KL-2018-201, Macassa deposit. Photograph by B. Dubé, NRCan photo 2023-403. **D.** Iron carbonate-altered plagioclase and amphibole diorite (*spotted porphyry*) along ddh UB-07-98 that was sampled for U-Pb geochronology at Upper Beaver. Photograph by B. Dubé, NRCan photo 2023-404. **E.** Sample CH-919-14-DAT-01 sampling area, Cheechoo deposit. Photograph by B. Dubé, NRCan photo 2023-405. **F.** Sample CH-919-14-DAT-01. Photograph by B. Dubé, NRCan photo 2023-406.

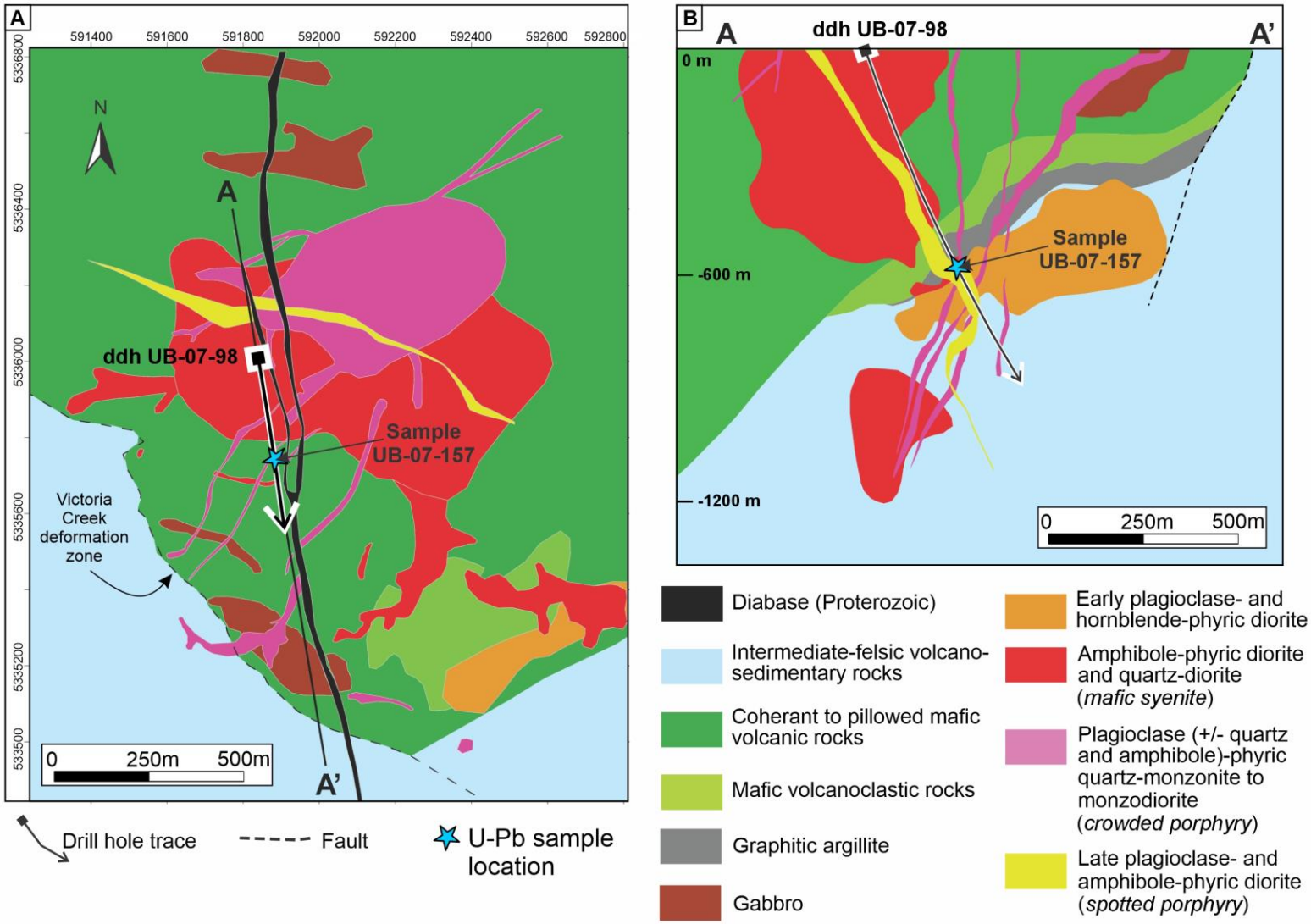

Figure 10. **A.** Simplified surface geologic map of the Upper Beaver deposit (spot 8 in Fig. 1) showing the trace of the sampled drill hole (UB-07-98) and location (projected to surface) of sample UB-07-157. **B.** Simplified geologic section looking East of the central part of the Upper Beaver deposit showing the trace of the sampled drill hole (UB-07-98) and location of sample UB-07-157 in the latest, and post-ore intrusive phase of the Upper Beaver complex. Figure courtesy of Agnico Eagle Mines limited.

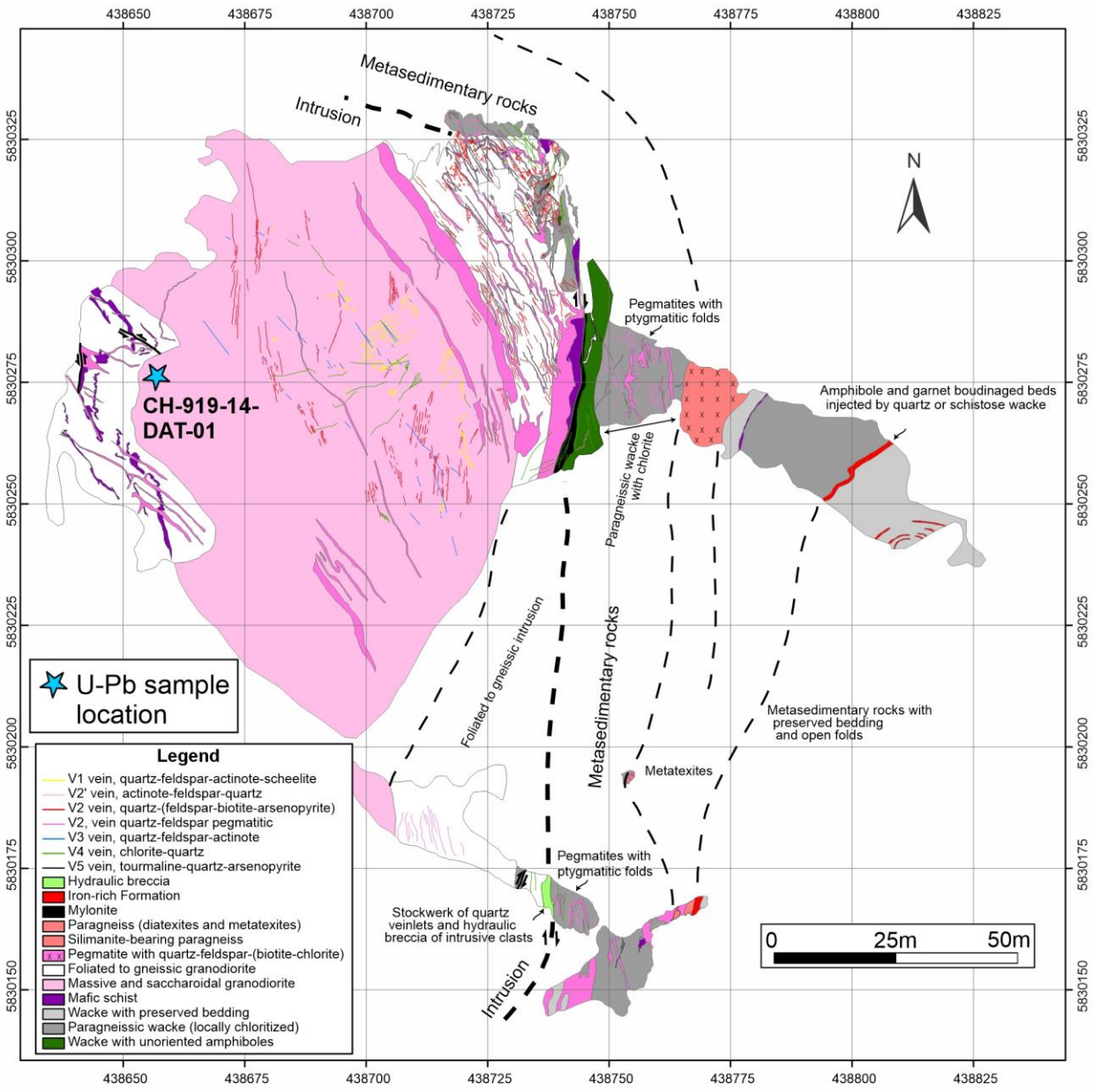

Figure 11. Geology of the main stripped area at the Cheechoo deposit showing the location of sample CH-919-14-DAT-01. Outcrop map from Fontaine et al. (2018). See Figure 2 for location of the Cheechoo deposit.

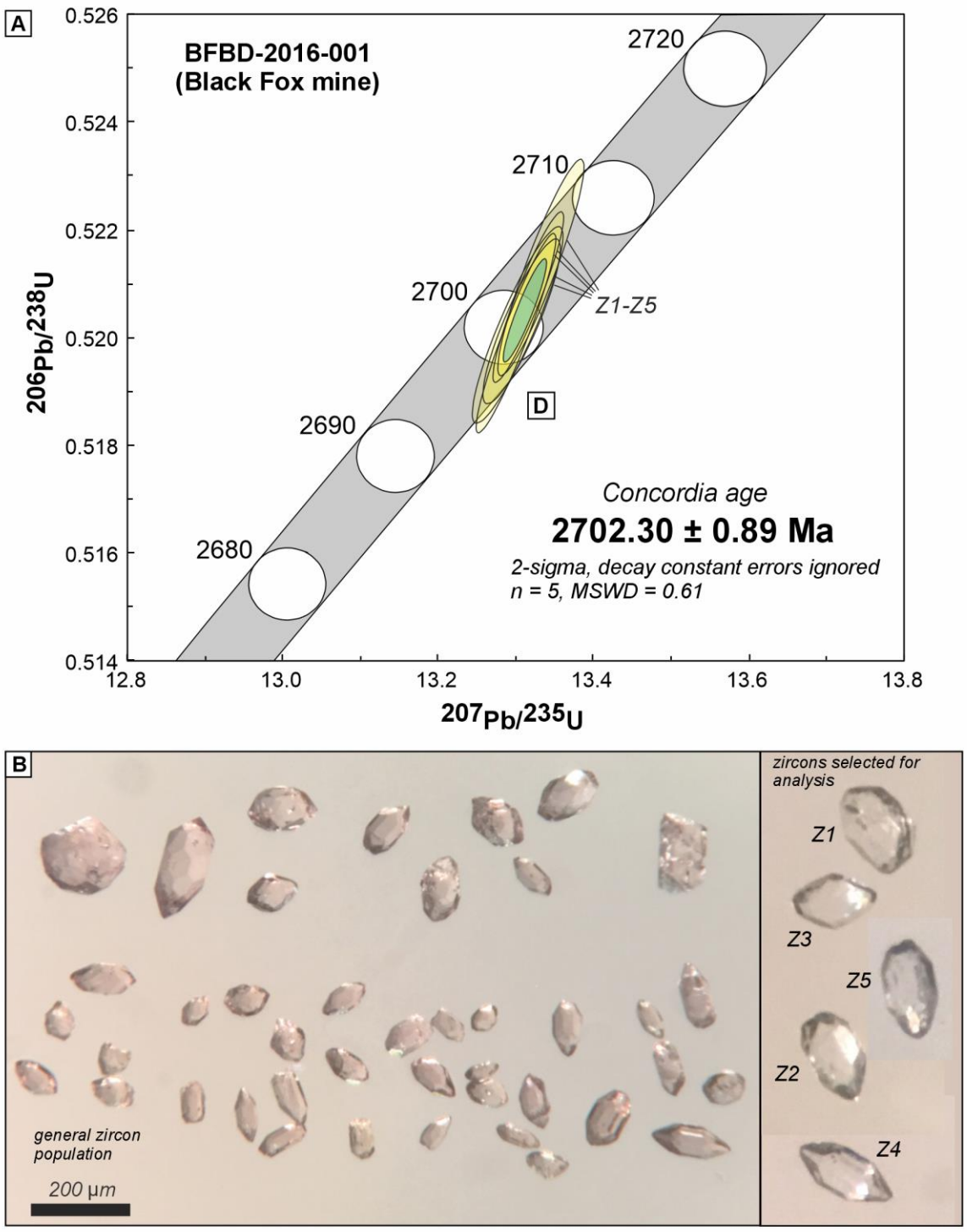

Figure 12. A. U-Pb Concordia diagram for sample BFBD-2016-001 (Blakc Fox mine - spot 3 in Fig. 1). Uncertainties are plotted at the 2σ level. Coloured ellipses are included in age calculations. **B.** Transmitted light image of representative zircons analyzed from the sample.

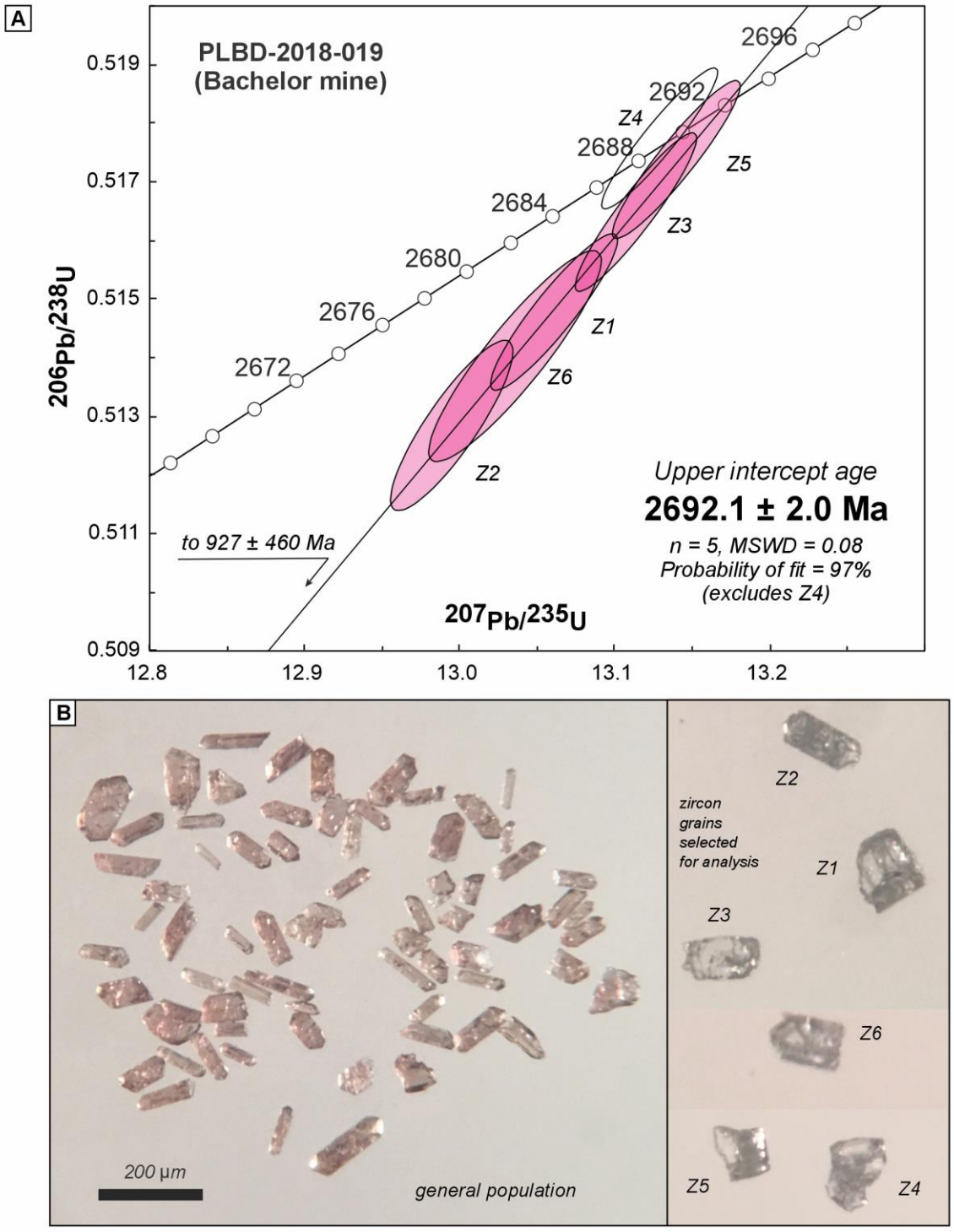

Figure 13. A. U-Pb Concordia diagram for sample PLBD-2018-019 (Bachelor mine - spot 1 in Fig. 1). Uncertainties are plotted at the 2σ level. Coloured ellipses are included in age calculations. **B.** Transmitted light image of representative zircons analyzed from the sample.

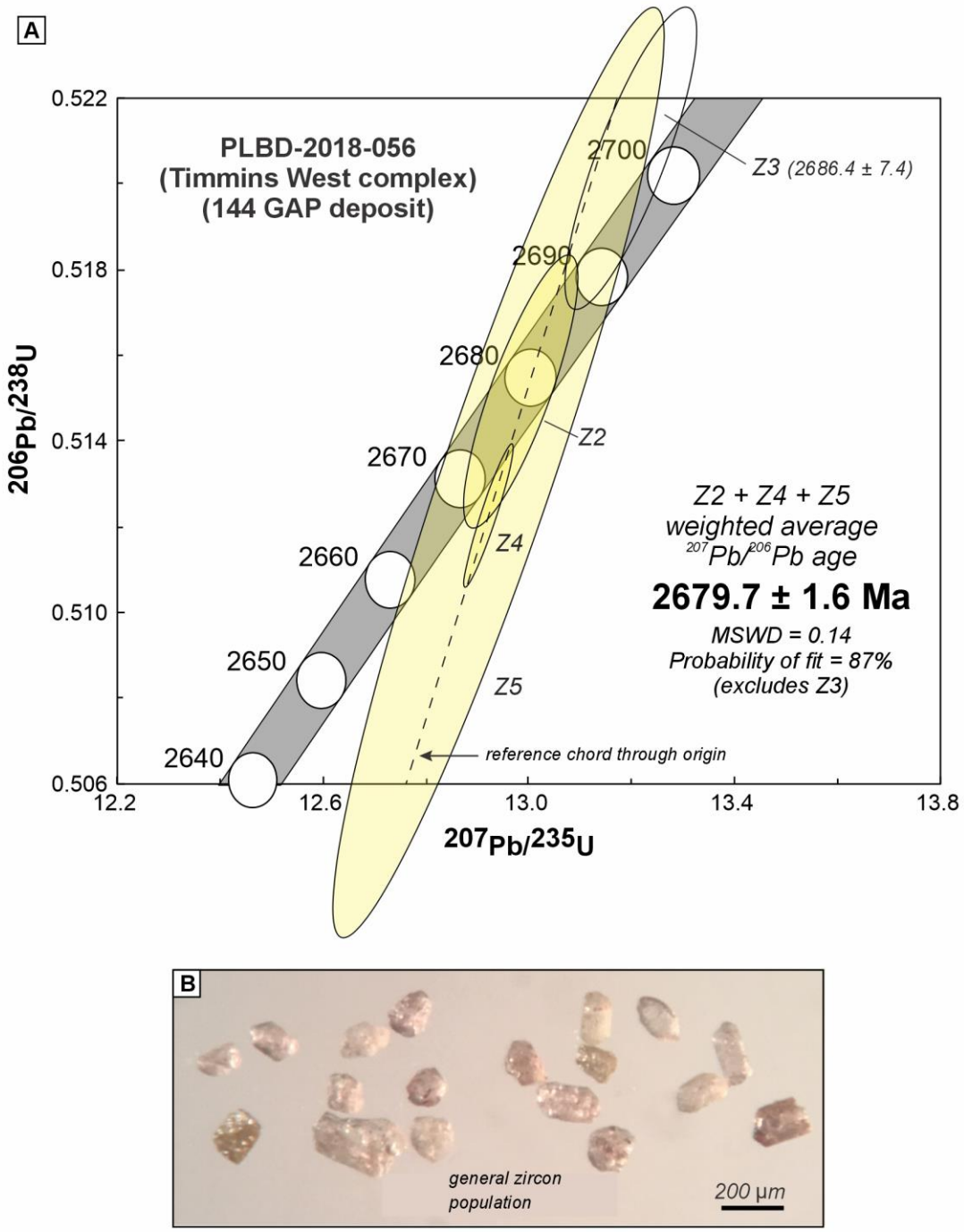

Figure 14. A. U-Pb Concordia diagram for sample PLBD-2018-056 (Timmins West complex - spot 4 in Fig. 1). Uncertainties are plotted at the 2σ level. Coloured ellipses are included in age calculations. **B.** Transmitted light image of representative zircons analyzed from the sample.

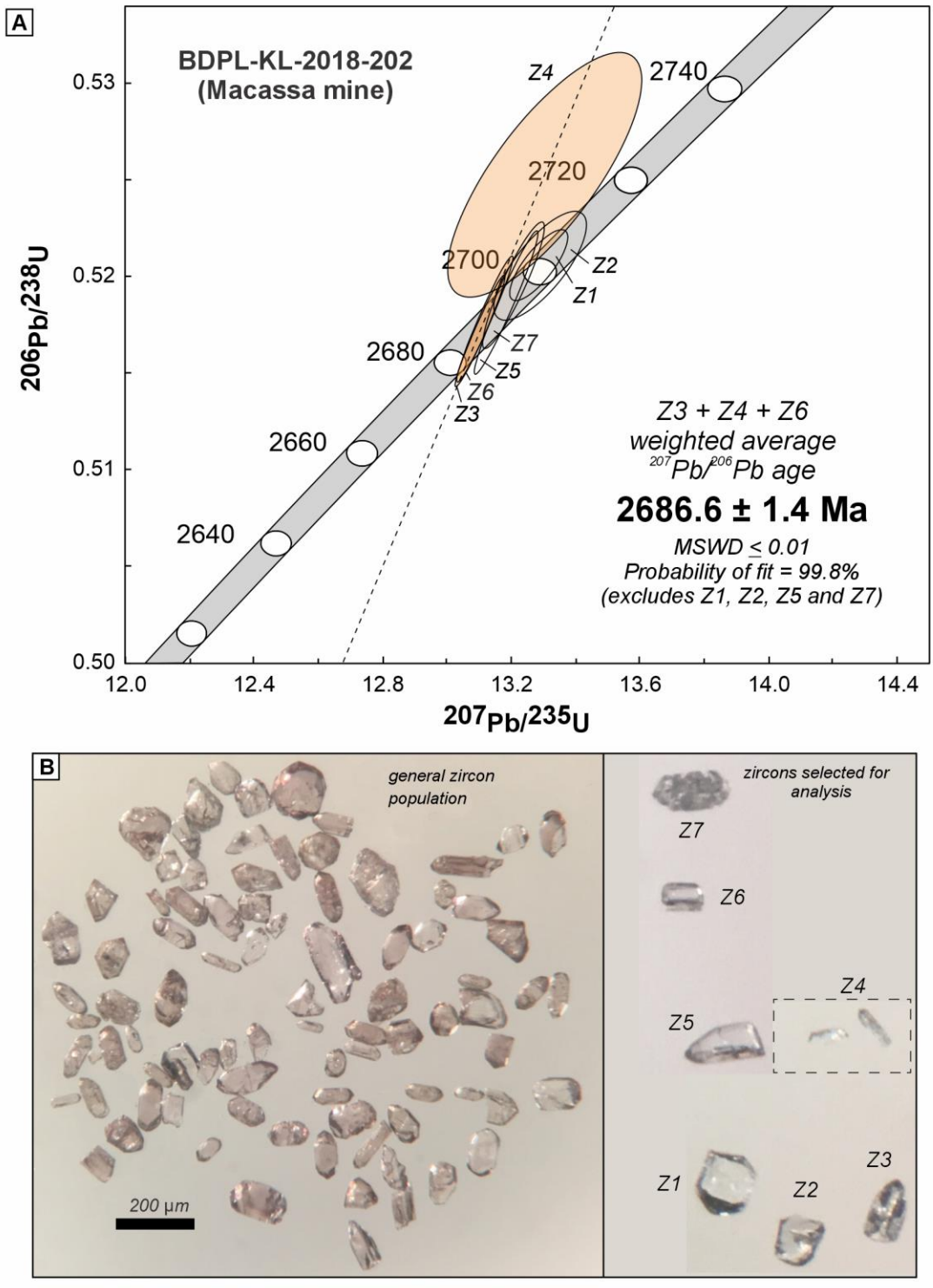

Figure 15. A. U-Pb Concordia diagram for sample BDPL-KL-2018-202 (Macassa mine - spot 6 in Fig. 1). Uncertainties are plotted at the 2σ level. Coloured ellipses are included in age calculations. **B.** Transmitted light image of representative zircons analyzed from the sample.

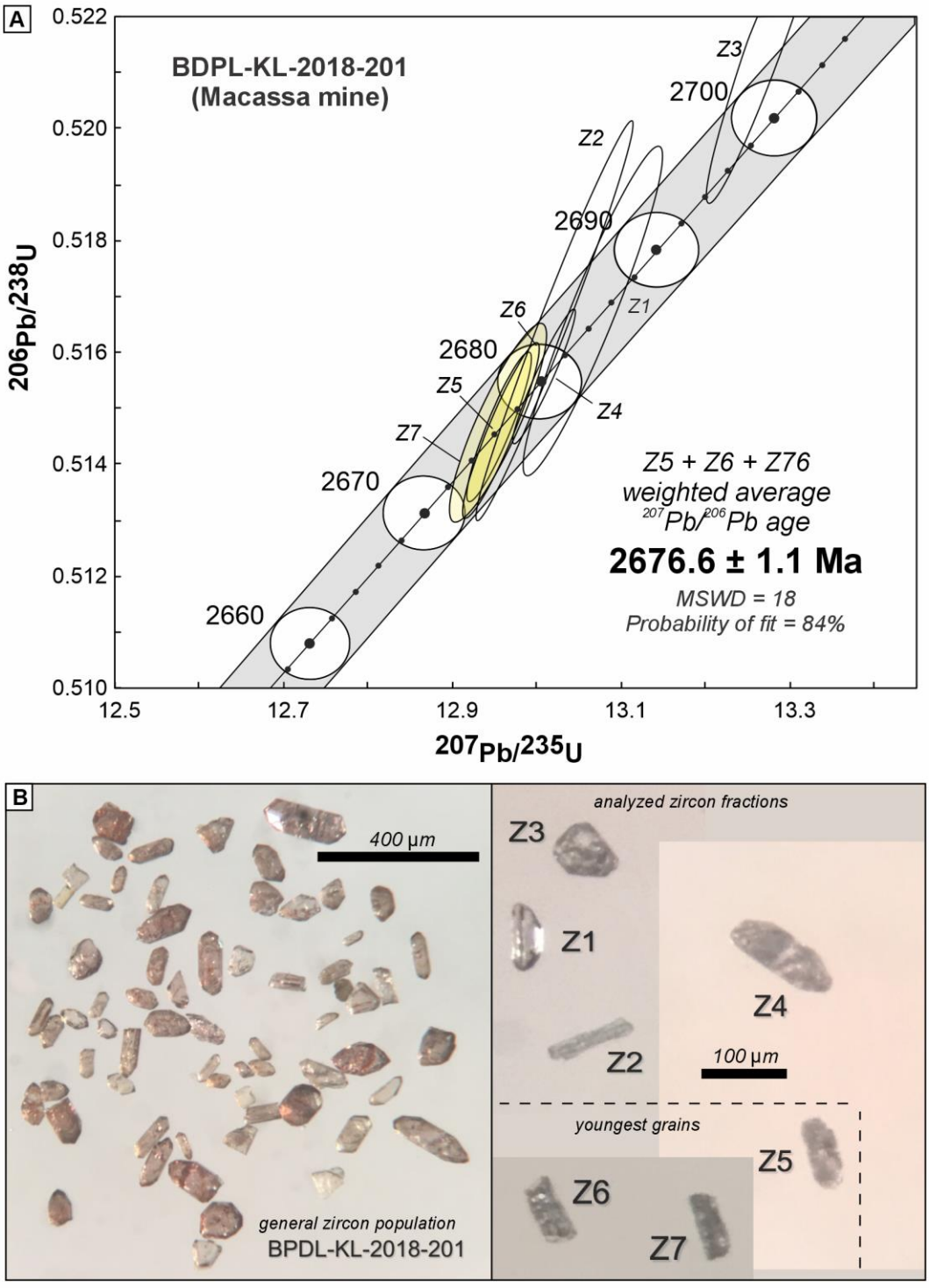

Figure 16. A. U-Pb Concordia diagram for sample BDPL-KL-2018-201 (Macassa mine - spot 7 in Fig. 1). Uncertainties are plotted at the 2σ level. Coloured ellipses are included in age calculations. **B.** Transmitted light image of representative zircons analyzed from the sample.

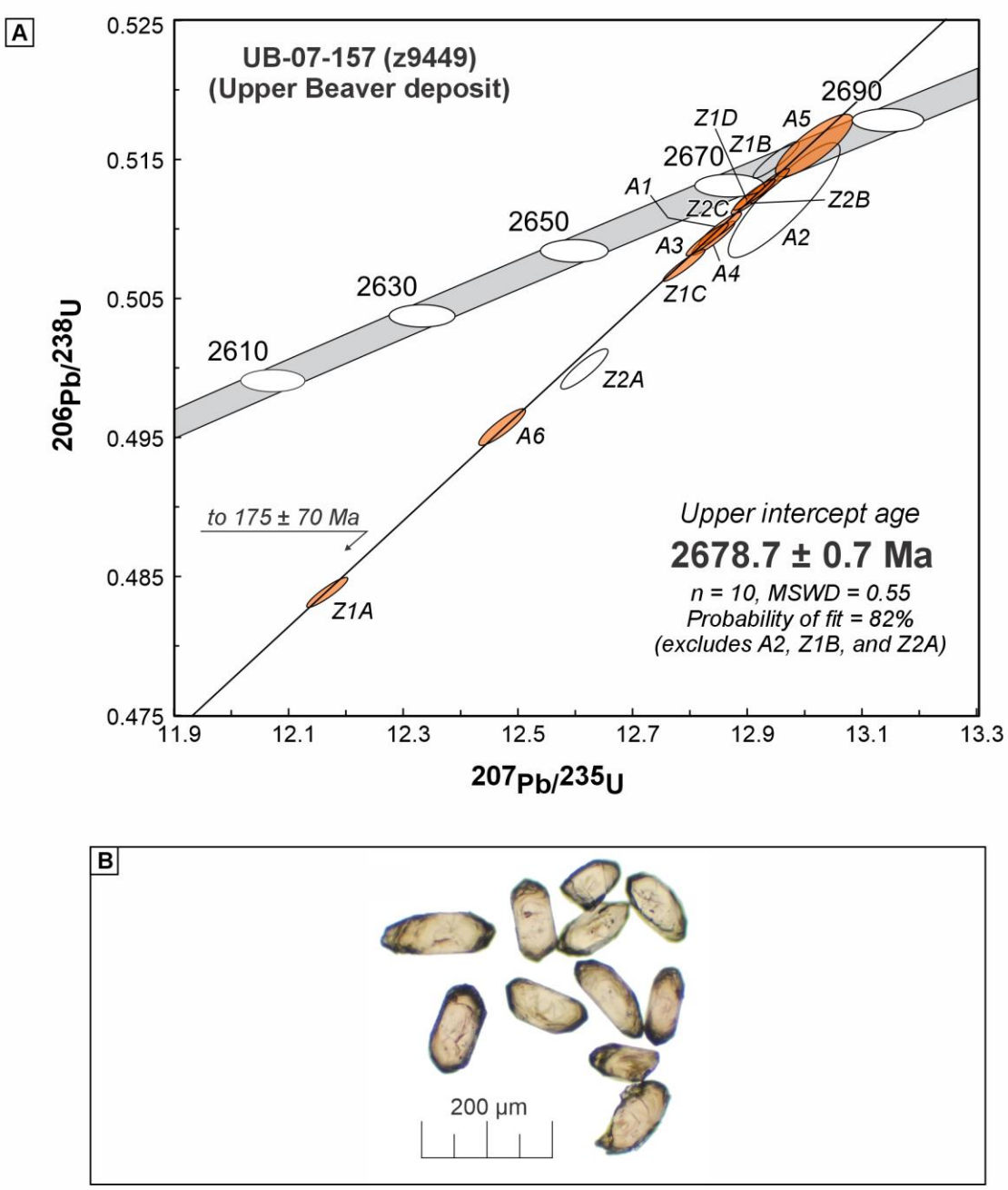

Figure 17. A. U-Pb Concordia diagram for sample UB-07-157 (Upper Beaver deposit - spot 8 in Fig. 1). Uncertainties are plotted at the 95% confidence level. Coloured ellipses are included in age calculation. **B.** Transmitted light image of representative zircon analyzed from the sample.

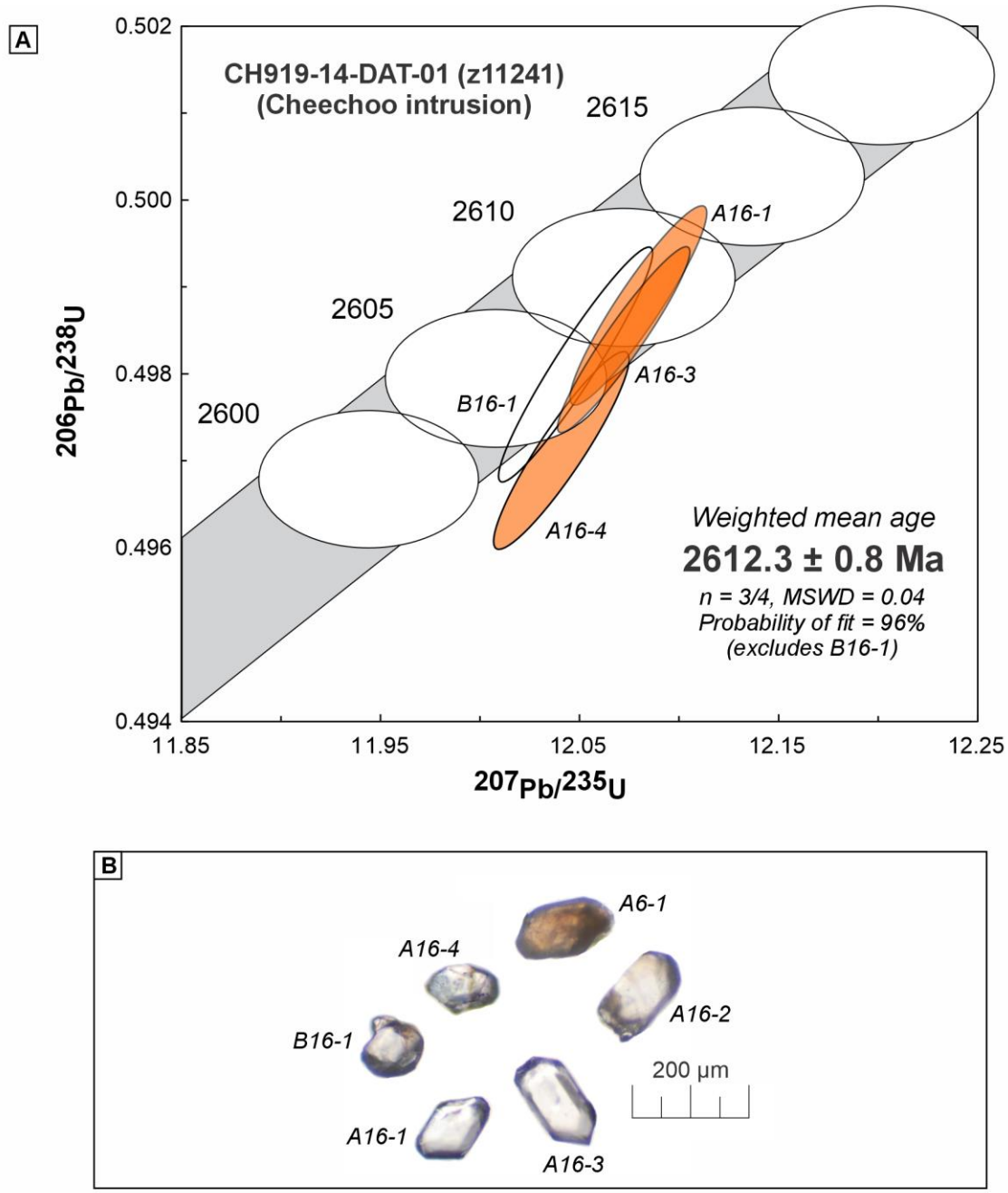

Figure 18. A. U-Pb Concordia diagram for sample CH919-14-DAT-01 (Cheechoo intrusion - see Figs. 2 and 11 for location). Highly discordant analysis A6-1 and inherited grain A16-2 are not plotted; see text for further details. Uncertainties are plotted at the 95% confidence level. Coloured ellipses are included in age calculation. **B.** Transmitted light image of representative, annealed zircon analyzed from the sample.